APPLICATION OF COMPLEX MODAL DECOMPOSITION METHODS TO DISPERSIVE MEDIA

By

Rickey Alfred Caldwell Jr.

A DISSERTATION

Submitted to
Michigan State University
in partial fulfillment of the requirements
for the degree of

Mechanical Engineering — Doctor of Philosophy

2016

ABSTRACT

APPLICATION OF COMPLEX MODAL DECOMPOSITION METHODS TO
DISPERSIVE MEDIA

By

Rickey Alfred Caldwell Jr.

Complex orthogonal decomposition (COD) is applied to an experimental beam to extract
the dispersive wave properties using response measurements. The beam is made of steel and
is rectangular with a constant cross section. One end of the beam is free and is hung by
a soft elastic cord. An impulse is applied to the free end. The other end is buried in
sand to absorb the wave as it travels from the impact site on the free-end; this effectively
prevents reflections of the wave off the buried end and emulates a semi-infinite beam. COD
is applied to the complex analytic displacement ensemble to obtain complex modal vectors
and associated complex modal coordinates. The spatial whirl rates of nearly harmonic modal
vectors are used to extract the modal wave numbers, and the temporal whirl rates of the
modal coordinates are used to estimate the modal frequencies. The relationship between the
frequencies and wave numbers are used to describe the dispersion relationships, which are
compared favorably to those of the theoretical infinite Euler-Bernoulli beam. Further efforts
are applied, and a new methodology is developed.

A novel method called smooth complex orthogonal decomposition (SCOD) is applied
to a simulated semi-infinite beam and the above instrumented experimental beam. These
measurements are converted into complex analytic displacements and velocities ensembles,
which are used to compute two correlation matrices. These correlation matrices form a
complex generalized eigenvalue problem whose eigenvalues and eigenvectors lead to the
extractions of the frequencies and wavenumbers of the constituent waves of the traveling

pulse. SCOD directly extracts the frequencies of the traveling waves from the eigenvalues. SCOD can extract the geometric relationship, phase velocity, and group velocity and agrees with analytical predictions. Applications of both methods are applied to a simulated infinite mass chain.

The dispersion relationship of a discrete chain of masses is extracted from numerically simulated data by applying complex modal decomposition. When an impulse excitation is applied to one end of a semi-infinite mass-spring chain, a wave is generated and propagates down the chain. This wave consists of various modes. The time record for the generated data is limited such that the wave reflection does not return to the sensed masses. For example, a 250-mass chain is simulated, and we consider (or sense) the time record of the first 100 masses. The data collected from the numerical simulation consists of the displacements of each mass at each time step. This data is then used to extract complex modes using COD and SCOD. The extracted complex modes accommodate modal traveling waves. We then compute the frequencies and wave numbers from modal coordinates and mode shapes, respectively. The amplitudes and frequencies of the modes are also estimated using Rayleigh quotients. The COD extracted dispersion relationship matches the analytical prediction of the dispersion curve for the linear mass chain.

I dedicate the completion of this achievement to all those who come before me. To those who endured much to create the opportunities I have today. To those who saw potential, who open doors for me or provided means for me to navigate obstacles, I recognize and thank you all. I will pick up and carry the torch as well.

ACKNOWLEDGMENTS

TABLE OF CONTENTS

LIST OF TABLES

LIST OF FIGURES

Chapter 1

Literature Review and Introduction

1.1 Literature Review

A great portion of this work focuses on waves traveling in infinite media, in particular, infinite Euler-Bernoulli (EB) beams, semi-infinite EB beams, and a semi-infinite mass chain. Euler first derived a model for beam oscillations in 1744 [1]. His work seemed to have been motivated by the questions of Bernoulli and is documented in letters between the two Swiss. Daniel Bernoulli published his works on the subject in 1751 [2] and today the EB beam model is still in use. The EB model assumes small deflections, negligible shear, and that planar cross sections remain plane. Another popular model is the Timoshenko beam model [3] which allows for the warping of cross sections and shear. It was developed in the early 20th century and is an extension of Euler's and Bernoulli's work.

Fourier was the first to derive the solution for the infinite EB beam with initial displacement and zero initial velocity [4]. Three and one-half score years later Boussinesq [5] derived a solution for the infinite EB beam with an initial velocity. Continuing in chronological order from Fourier, Graff [6] notes that in 1822 Cauchy developed elastic theory and the equations of motions for elastic solids. Efforts to find the original papers were thwarted by a language barrier as most of Cauchy's papers were in German. Graff also states the Poisson

published work describing waves in elastic media in 1828. Poisson (1828) [7] and Cauchy were able to get similar results. Efforts to describe waves in solids continued. The next noteworthy development relating to this subject was Pochammer's who developed frequency relationships for waves traveling in rods. Later, Rayleigh's work on surface waves in 1885 [8] predicted the existence of what are called Rayleigh-Lamb waves. Physically, these waves travel near the surface of thick plates. A common example are earthquake waves. Lamb published considerable works on group velocities and waves in plates [9, 10]. These works were furthered by Pao and Mindlin [11] in the 1960's.

Jumping back to the early 1940's, work in statistics and fluid dynamics would lend itself to structural analysis. Proper orthogonal decomposition (POD) is a statistical tool developed independently by many different people from all over the globe spanning from 1943 to 1955; the progenitors include Kosambi, Karhunen, Pougachev, Oboukhov [12, 13] and Lumley [14]. POD is a tool for statistically separating two independent variables such as time and space. POD has equivalent formulations such as principal component analysis, Karhunen-Loéve decomposition (KLD), empirical orthogonal function (EOF) [15], and singular value decomposition (SVD) [13, 16]. POD was initially applied to characterize spatial structures in fluid flows, particularly turbulent flows, turbulent flows around objects, and turbulent flows near boundaries [14, 17–20], and now is used in many fields such as controls [21–24], signal processing, thermo-fluids [25, 26], finance [27] and structures [28, 29]. Among the structural applications, modal analysis and nondestructive evaluation have received a great deal of attention [29–31].

In the realm of modal analysis, POD is used to extract linear normal modes (LNMs) from discrete and continuous systems [32–34] excited by a modal impact hammer or by

2

random excitation [35]. Improvements were sought and other methods based on POD were developed such as enhanced POD [33], reduce-order mass-weighted POD [33, 36], and many more. New formulations with additional ensembles were developed such as smooth orthogonal decoosition (SOD) by Chelidze and Zhou in 2006 [37] and similarly the smooth Karhunen-Loeve decomposition (SKLD) in 2009 by Bellizzi and Sampaio [38]. A benefit of SOD is that *a priori* knowledge of the mass matrix is not needed and mode shapes and frequencies can be directly extracted [37, 39, 40]; and damping ratio if using SKLD [38]. This differs from POD in which requires computing the fast Fourier transform of the modal coordinates to extract natural frequencies, and using logarithmic decrement on the modal coordinates to extract damping.

The idea of POD in the complex plane was develop and published simultaneously by Georgiou and Papadopoulos in 2006 [41], called C-POD, and by Feeny at the ASME IMECE conference, later published and called the complex orthogonal decomposition (COD) in [42]. COD was used to decompose wave motion into its primary components and parameters such as wavenumber, frequency, phase velocity, and group velocity. Additionally, with COD, traveling and standing waves could be discerned, and the degree of traveling waves could be quantified using the traveling or synchronicity index [43]. Feeny et al applied COD to bio-locomotion of nematode worms [44] in 2009 and of fish in [45] and was able to discern different mechanism used by the organism to travel forward, backwards, and to turn. Esquivel [15] applied COD to simulated data and power system data to measure fluctuations in power systems in 2009. COD is well suited to describe fluctuations in space and time. When related to wave velocity this relationship is called the dispersion relationship.

This research starts with the verification of [46] with a beam experiment and creates a new formulation related to COD and SOD, which allows for the direct extractions of wavenumbers and frequencies. This formulation is called smooth complex orthogonal decomposition (SCOD) and is applied to a simulation, beam experiment, and to a simulated infinite mass chain.

1.2 Introduction

Waves are ubiquitous. Pressure waves as sound and electromagnetic waves that we see as light, are just of two examples of waves. Mechanical waves (like sound) and stress waves, requires a medium to travel from point A to point B. These waves can be of great engineering importance, and understanding how they propagate is critical. For example, waves from explosions at construction sites and in mines are used to loosen and remove material from a localized area. That same explosive force is used in improvised explosive devices (IEDs) or as a tool for terrorist which can cause injury, death, and destruction of property. Efforts have been made to understand how these blast waves interact with the human body, and how to mitigate these waves to prevent damage to human tissue and property. However, waves used for good can assist in such things as locating buried mines, in diagnostic devices in the medical field (magnetic resonance imaging, X-rays, ultrasound), nondestructive evaluation and testing, or in archaeologically to find buried ruins using ground penetrating radar. All of these modern equipment are possible by understanding waves and how waves interact with objects. The tools developed in this dissertation can be used to characterize how waves interact with objects.

The objective of this dissertation is to use measured responses to define the geometric dispersion relation (GDR) in engineering structures. Dispersion relationships are equations that describe the relationship between frequency (ω), wavenumber (k), geometry, and material properties. Examples of different systems and their geometric relationships are in Table 1.1 below: (a) waves traveling through the Earth's core [47], where B_s is the radial component (cylindrical coordinate system) of the magnetic field, μ_0 is permeability of free space, and ρ_0 is the reference density. Example (b) describes ripples traveling on the surface of a shallow pond [48], where $\mu = \dfrac{h_0^2}{6\lambda_0^2}$ is a non-dimensional parameter h_0 is undisturbed water depth and λ_0 is the typical wavelength. Example (c) is light through a prism, where c is the speed of light in a vacuum, and n is the refractive index. Example (d) is flexure waves in a beam, where E is the modulus of elasticity, I is area moment of inertia of the cross-section, ρ is the mass per unit length of the beam, and A is the cross-sectional area. Along with each system is its GDR, from which the phase velocity and the group velocity can be determined. The phase velocity, c_p, is the velocity of a point on a single-harmonic wave in space, for example, a single peak. The group velocity, c_g, is the velocity of the envelope of a group of waves. The equations for the two velocities are $c_p = \omega/k$ and $c_g = d\omega/dk$. Dispersion is a characteristic where group or phase velocity is dependent on the frequency. Examples (a) and (c) are non-dispersive example (b) and (d) are dispersive.

Specifically, we will use COD and SCOD to estimate the wavenumber, k, and frequency, ω, of the constituent waves traveling in a simulated and experimental beam, and a 100 mass, mass-chain system. From the wavenumbers and frequencies, we can determine the GDR, the phase velocity, and group velocity of each system.

Example	Dispersion Relationship	Phase velocity	Group velocity
(a)	$\omega = k\sqrt{\dfrac{B_s^2}{\mu_0 \rho_0}}$	$c_p = \sqrt{\dfrac{B_s^2}{\mu_0 \rho_0}}$	$c_g = \sqrt{\dfrac{B_s^2}{\mu_0 \rho_0}}$
(b)	$\omega = k - 4\pi^2 \mu k^3$	$c_p = 1 - 4\pi^2 \mu k^2$	$c_g = 1 - 12\pi^2 \mu k^2$
(c)	$\omega = ck$	$c_p = c/n$	$c_g = c\omega/(n\omega + ck)$
(d)	$\omega = k^2\sqrt{\dfrac{EI}{\rho A}}$	$c_p = k\sqrt{\dfrac{EI}{\rho A}}$	$c_g = 2k\sqrt{\dfrac{EI}{\rho A}}$

Table 1.1: Examples of geometric dispersion equations, phase velocities, and group velocities, in (a) waves traveling through the Earth's core, (b) ripples on a pond, (c) light waves through a prism, and (d) flexure in a uniform beam. In example (a) the phase and group velocity are equal. In (c), the group velocity is slower than the phase velocity. In (d), the group velocity is faster than the phase velocity.

To provide a foundational understanding a brief review of waves in a Euler-Bernoulli beam, Rayleigh's quotients, and proper orthogonal decomposition (POD) will be presented first.

1.3 Background

A brief introductions to the major concepts and tools used in this research will be briefly reviewed. First, the equations of motions for a uniform Euler-Bernoulli beam will solved for simple harmonic waves. The results of this will lead to the dispersion relationship. Examples of dispersion relationship for different types of systems will be presented as well as parameters derived from the dispersion relationship call the group velocity and the phase velocity. Together the dispersion relationship, group velocity, and phase velocity are the properties this research seek to measure in using COD and SCOD.

1.3.1   Waves in a Euler-Bernoulli Beam

The derivation of the Euler-Bernoulli beam equation is well known and can be found in most vibration-theory textbooks such as [49], and will not be reviewed. The equation of motion for a uniform Euler-Bernoulli beam (EB) is

$$\rho A \ddot{y}(x,t) + EI \frac{\partial^4}{\partial x^4}[y(x,t)] = 0, \tag{1.1}$$

where x is the position along the beam, t is time, $y(x,t)$ is the transverse displacement, ρ is the mass density, A is the area of beam's cross-section, E is the modulus of elasticity, and I is the area moment of inertia of the beam's cross-section about the neutral axis. To understand how traveling waves behave in an EB let's substitute a solution to the wave equation into the Euler-Bernoulli beam equation.

Following Graff [6], inserting

$$y(x,t) = e^{i(kx - \omega t)}, \tag{1.2}$$

which is a wave traveling in the positive x-direction, into Eqn. (1.1), and solving for ω, leads to the geometric dispersion relationship

$$\omega = ak^2, \tag{1.3}$$

7

where

$$a = \sqrt{\frac{EI}{\rho A}}. \tag{1.4}$$

In Eqn. (1.3) ω is the temporal frequency with units of rad/s, and k is the spatial frequency measured in units of rad/m. This equation describes the relationship between the frequency and wave number of a wave traveling through a uniform homogeneous Euler-Bernoulli beam. The phase velocity and group velocity are derived from the geometric dispersion relationship.

The phase velocity is defined as $c_p = \omega/k$ and for the Euler-Bernoulli beam that is equal to $c = ak$. For the EB beam the speed of a propagating harmonic wave increases linearly with its wave number. This phase velocity due to the dispersion relationship is quadratic. Other systems may have constant phase velocity of the form $c = a$. The group velocity is defined as $c_g = d\omega/dk$. For the EB beam the group velocity is $c_g = 2ak$. The group velocity is twice the phase velocity for the EB beam. Phase and group velocities for different systems can be equal, positive and unequal, or have opposite signs.

In solving the partial differential equation (PDE) in Eqn. (1.1) separation of variables is used as a standard technique, which leads to an eigenvalue problem (EVP). Eigenvalue problems (EVP) or a generalized eigenvalue problems (GEVP) are used extensively in this work. They appear in the solving of Eqn. (1.1), POD, SOD, COD, and SCOD. Rayleigh's quotient is an import tool for making approximations based on an EVP. Therefore, a brief overview of these topics follows.

1.3.2   The Eigenvalue Problem and Rayleigh's Quotient

A terse review of the properties of eigenvalue problems is needed. A eigenvalue problem (EVP) has the form

$$\mathbf{A}\mathbf{v} = \lambda\mathbf{v} \tag{1.5}$$

where $\mathbf{A}$ is a square matrix, $\mathbf{v}$ is called the eigenvector, and λ is a scalar called the eigenvalue. The eigenvector is a characteristic vector of $\mathbf{A}$ with the property that when $\mathbf{A}$ operates on $\mathbf{v}$ the output is a scalar multiple of $\mathbf{v}$, as indicated in Eqn. (1.5). Geometrically, when $\mathbf{A}$ performs a transformation on $\mathbf{v}$ the resulting transformation can only change $\mathbf{v}$ in length and direction (sign, $\pm$) and not the orientation of $\mathbf{v}$. (In some cases, however, λ and $\mathbf{v}$ are complex, and their real scaling property is not obvious in the real space, as the complex action is reflected in real space as a rotation.)

Some properties of the EVP are discussed here. If $\mathbf{A}$ is real, then the eigenvalues are real or have complex conjugate pairs. Each complex conjugate pair of eigenvalues have a corresponding complex conjugate pair of eigenvectors. If $\mathbf{A}$ is symmetric ($\mathbf{A}^T = \mathbf{A}$) and positive semi-definite, its eigenvalues are $\lambda_i \geq 0$. If the rank of $\mathbf{A}$ is full (positive definite case) and the eigenvalues are distinct, then the eigenvectors form a basis for $\mathbf{A}$. Also, if each eigenvector is normalized to unit length, then the eigenvectors form an orthonormal basis for $\mathbf{A}$ such that $\mathbf{v}_i\mathbf{v}_j = \delta_{ij}$, where δ_{ij} is the Kronecker delta. The eigenvectors plus $\mathbf{v} = \mathbf{0}$ creates the eigenspace of $\mathbf{A}$. If an eigenvalue is equal to 0 then the matrix is singular and noninvertible.

Returning to the original EVP in Eqn. (1.5) for a particular eigenvalue $\mathbf{v}_i$, pre-multiplying by $\mathbf{v}_i^T$ leads to $\mathbf{v}_i^T \mathbf{A} \mathbf{v}_i = \lambda_i \mathbf{v}_i^T \mathbf{v}_i$ such that

$$\lambda_i = \frac{\mathbf{v}_i^T \mathbf{A} \mathbf{v}_i}{\mathbf{v}_i^T \mathbf{v}_i}. \tag{1.6}$$

This ratio can be constructed using an arbitrary vector, $\mathbf{u}_i$, defining the Rayleigh's quotient (RQ) as

$$R(\mathbf{A}, \mathbf{u}) = \frac{\mathbf{u}^T \mathbf{A} \mathbf{u}}{\mathbf{u}^T \mathbf{u}}.$$

Then it is clear from Eqn. (1.6) that $\lambda_i = R(\mathbf{A}, \mathbf{v}_i)$. It can be shown that the values of the RQ are stationary in the neighborhoods of eigenvectors [50], and that value of the RQ is bounded by the highest and lowest eigenvalues, such that $\min(\lambda_i) \leq R(\mathbf{A}, \mathbf{v}) \leq \max(\lambda_i)$. Thus the RQ is a good way to approximate eigenvalues given an assumed eigenvector.

A generalized EVP has the form,

$$\lambda \mathbf{A} \mathbf{v} = \mathbf{B} \mathbf{v}. \tag{1.7}$$

Some properties of the GEVP we now review. If $\mathbf{B}$ is invertible then $\mathbf{B}^{-1} \mathbf{A} \mathbf{v} = \alpha \mathbf{v}$ where $\alpha = 1/\lambda$. In this case, the GEVP will have all the properties of the EVP. Also, if $\mathbf{A}$ is invertible then $\lambda \mathbf{v} = \mathbf{A}^{-1} \mathbf{B}$. If $\mathbf{A}$ is real and symmetric and $\mathbf{B}$ is real, symmetric and positive definite (although $\mathbf{A}^{-1} \mathbf{B}$ and $\mathbf{B}^{-1} \mathbf{A}$ are not symmetric) then all n eigenvalues are real, and the eigenvectors are orthogonal through $\mathbf{B}$ so that $\mathbf{v}_i \mathbf{B} \mathbf{v}_j = \delta_{ij}$. The eigenvector is

any vector that, when transformed by $\mathbf{A}$ and $\mathbf{B}$, the resulting vectors of both transformations are collinear. The RQ of a GEVP is defined as

$$\lambda_i = R(\mathbf{A}, \mathbf{B}, \mathbf{v}) = \frac{\mathbf{v}_i^T \mathbf{B} \mathbf{v}_i}{\mathbf{v}_i^T \mathbf{A} \mathbf{v}_i}. \tag{1.8}$$

For both the EVP and the GEVP if $\mathbf{A}$ or $\mathbf{B}$ is complex then T, the transpose, is replaced with H, the Hermitian operation, or the complex conjugate transpose.

1.3.3 Proper Orthogonal Decomposition

This thesis makes use of methods that are generalizations of proper orthogonal decomposition (POD). Hence, POD is introduced here for background. POD was first used in mechanics by Lumley to study turbulence in fluid dynamics [14]. Later Berkooz et al. [17] reviewed the properties of POD for turbulence. POD was applied to structural dynamics [51–53], and later to extract modal parameters [32,44,54,55]. POD is an important and widely used tool. For example, an ISI citation search on November 2015, yields more than 2900 papers. POD is equivalent to singular value decomposition (SVD) [16,55–57]. It has several different variations for the extraction of different parameters of interest. These variations include mass-weighted reduced order proper orthogonal decomposition [36,40], Ibrahim time-domain decomposition [58], smooth orthogonal decomposition (SOD) [37,39,40], state-variable modal decomposition (SVMD) [59] and, complex orthogonal decomposition (COD) [46,60].

To apply POD to a structure the experimenter senses a structure and captures response signals (for example displacements) at different points simultaneously on the structure during

its response to some type of excitation, for example an impulse [54]. Next an ensemble matrix, $\mathbf{X} \in \mathbb{R}^{M \times N}$, is created from the sensor measurements, where M is the number of sensors and N is the number of time samples taken. Specifically, $\mathbf{X} = \begin{bmatrix} \mathbf{x}_1^T \ \mathbf{x}_2^T \ \cdots \mathbf{x}_M^T \end{bmatrix}^T$, where $\mathbf{x}_i = [\mathbf{x}_i(0) \ \mathbf{x}_i(\Delta T) \ \mathbf{x}_i(2\Delta T) \ \cdots \mathbf{x}_i((N-1)\Delta T)]^T$, such that each row of the ensemble matrix is the data from one sensor and the index of each column is a single measurement sample:

$$\mathbf{X} = \begin{bmatrix} x_1(0) & x_1(\Delta t) & \cdots & x_1((N-1)\Delta t) \\ x_2(0) & x_2(\Delta t) & \cdots & x_2((N-1)\Delta t) \\ \vdots & \vdots & \ddots & \vdots \\ x_M(0) & x_M(\Delta t) & \cdots & x_M((N-1)\Delta t) \end{bmatrix}$$

Often the mean is subtracted from each sensor's time history.

Next a correlation matrix, $\mathbf{R} = \dfrac{\mathbf{X}\mathbf{X}^T}{N}$, is computed, such that $\mathbf{R} \in \mathbb{R}^{M \times M}$. Finally, an eigenvalue problem is formulated as $\mathbf{R}\mathbf{v} = \lambda\mathbf{v}$. The eigenvectors are called proper orthogonal modes (POMs) and for lightly damped structures vibrating in the linear elastic range with a mass matrix proportional to the identity, the POMs converge to linear normal modes (LNMs) [32, 55, 61]. The eigenvalues are called proper orthogonal values (POVs) and relate to modal energy [17, 44]. The natural frequencies of the beam can be estimated from the proper orthogonal modal coordinates (POC) defined as $q_i = \mathbf{v}^T\mathbf{X}$. Typically the fast Fourier transform (FFT) of the POC are used to estimate the frequency of each mode.

Complex orthogonal decomposition and a complex version of smooth orthogonal decomposition are to be applied in this research, and will be discussed later.

1.4   Thesis Preview

There are six remaining chapters in this body of work. Chapter 2 describes the beam experiment. The experimental setup is based on the prior work of Önsay and Haddow [62]. The goal of the experiment was to create a testing rig which allowed waves, generated from an impact, to travel down a beam and not reflect off of one of the free ends. This was done to emulate a semi-infinite beam. Chapter 3 introduces COD and the application of COD to a beam experiment. Alternative formulations were sought to achieve direct computation of wavenumbers and frequencies. In Chapter 4 a novel decomposition method was created called the smooth complex orthogonal decomposition (SCOD). SCOD is formulated in the time domain to directly compute frequencies. Then in Chapter 5, SCOD is cast in the spatial domain to directly compute wavenumbers. Finally, chapter 6 applies both COD and SCOD to a mass-chain system to explore their capability on linear mass chain.

1.5   Contributions

Contributions to the field covered in this thesis include applying COD to a beam experiment. This reinforces the simulation done in prior work, and shows that COD can extract the dispersion relationship from a beam in real world conditions on real systems. By developing SCOD several contributions were made. First, a theoretical framework for SCOD has been established. Second direct frequency estimation from an eigenvalue problem can be made. COD and SCOD together are new tools for wave propagation analysis and contribute to the state-of-the-art. The study on a mass chain system contributes the science of dispersion in particles and lumped-mass systems, offers insights and a tool for extracting a dispersion relationship in lattice system with application in meta materials.

Chapter 2

Beam Experiment

This experiment is similar in setup to an experiment conducted by Önsay and Haddow [62] in which they used a wavelet transform to extract the properties of a wave traveling in an elastic medium. In this experiment one end of a beam was partially buried in coarse unpacked sand and the other end of the beam was suspended freely with an elastic cord. The beam was sensed with 31 accelerometers placed equidistantly on the unburied part of the beam. The beam was struck with a mini impact hammer near the free end. As the impulse waves traveled along the beam, starting at impact location near the free end and moved towards the sandbox, the waves were sensed by each accelerometer as they propagated. Once the waves reached the buried end, the sand absorbed the waves, which resulted in anechoic termination. What follows is a detailed description of the experiment along with the purpose of the design.

2.1 Equipment

The data acquisition (DAQ) equipment is listed in Table 2.1. The National Instruments DAQ system had 32 available channels, an express PCI card which was connected to a DELL Inspiron laptop computer running a 32 bit Windows XP operating system, and was linked to the NI Chassis via a controller card. Two DAQ cards were plugged into the chassis. Each card had an 16 channel capacity. The sampling rate was set to 25 kHz based on the

maximum measurable wavenumber (as explained in the section on data processing). The maximum sampling rate of the DAQ system was 32 kHz. Thirty-one channels were used for accelerometers, and one channel was used for the impact hammer. Although the impact hammer was not used in any of the output only decomposition method computations, seeing the impact data helped to ensure quality results by having the capability of inspecting for bad impacts (for example, double taps, sliding, sensor saturation, and non-impulsive waves). The number of channels limited the spatial resolution of the beam experiment.
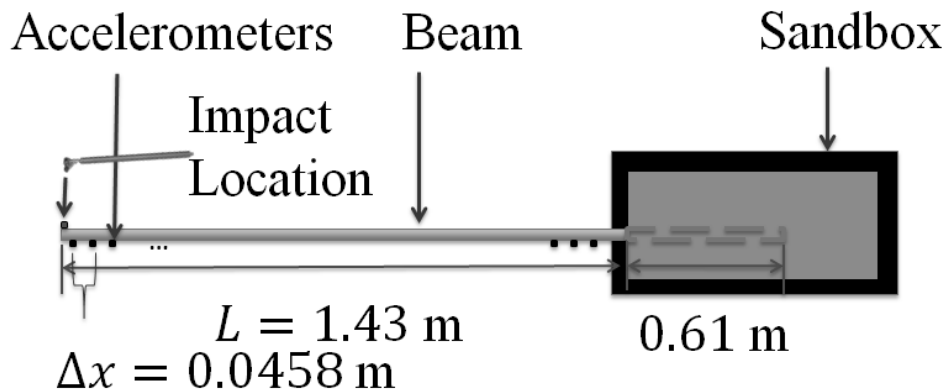
Figure 2.1: Experimental setup.

Data Acquisition Equipment	
Chassis	NI PXI-1042Q
Cards	
PCI express card	NI PXI - 8360
DAQ card	NI PXI - 4496
Controller card	NI PXI - 8361
Accelerometer	PCB 352B10
Accelerometer mass	0.0007 kg
Impact hammer	PCB model 086C80
Hammer tips	
Flat metal	PCB model 084B03
Vinyl cap	PCB model 085A07
Pointed metal cone	unknown

Table 2.1: Data Acquisition System

2.2   Beam

The experimental beam was made of carbon steel, and its dimensions are listed in Table 2.2. The beam was cleaned with sandpaper and wiped down with acetone to remove rust and chemical residues. One end of the beam was supported by an elastic cord and the other end was buried in sand as shown in Figure 2.1. The sand was playground sand purchased at Home Depot. The box that held the sand was made from 1/4 inch oriented strain board (OSB) plywood boards. The dimensions of the box were 3 ft × 1 ft × 1 ft. A 1/2 inch slot was cut into the 1 ft × 1 ft face of the box which was used to insert the beam into the sand. Care was taken to ensure that the beam was suspended in the sand and did not touch the box. The total beam length was 2.038 m of which 0.61 m was buried in the sand. The remaining 1.43 m unburied portion of the beam was sensed with accelerometers. The accelerometers were attached with bee's wax along the neutral axis of the beam, 0.0458 m apart, for a total sensor network length of 1.42 m. The mass of each accelerometer was 0.0007 kg.

Experimental Beam Dimensions	
Length	2.038 m
Base	0.069 m
Height	0.0045 m
Density	7870 kg/m^3
Modulus of Elasticity	200 GPa

Table 2.2: Beam Dimensions

2.3   Procedure

The beam was tapped lightly with the mini impact hammer, such that the first bending mode was not visibly detected with the naked eye. The impulse traveled down the beam, and the

induced accelerations were detected and measured by the accelerometers and recorded by the data acquisition system.

2.4 Data Processing

The data included 100 samples before the hammer impact and 300 samples after the impact for a total of 400 samples. First, the data from each sensor was filtered forward and backward with a high-pass filter with a cutoff frequency of 100 Hz. Second, the mean of each sensor's time history was subtracted from its samples using Matlab's `"detrend"` with a `"constant"` modifier. Third, any linear trends in time were removed using the same command as above with a `"linear"` modifier. Fourth, the signals were translated on the time axis such that the sample before the hammer impact had a time and force value of zero. Finally, the first and last 100 samples were truncated leaving the start of the impact plus 200 samples. Accelerations signals are shown in Figure 2.2 and Figure 2.3.

To get velocities, the signals were numerically integrated using the `"cumtrapz"` command. The means were subtracted from the velocities, which were then high pass filtered to remove low frequency integration drift, and integrated once more to get displacements. The velocities are shown in Figure 2.4 and Figure 2.5. The means were subtracted from the displacements, and the displacements were filtered for a final time. The displacements are pictured in Figure 2.6 and Figure 2.7.

Based on the sampling rate of rate $f = 25{,}000$ Hz and time record of $N/f = 0.008$ s, the maximum detectable frequency is $f_{max_t} = 12{,}500$ Hz and the minimum detectable frequency

is $f_{min_t} = 125$ Hz. The minimum detectable wave number is defined by the span of sensors, L, such that $k_{min_s} = \dfrac{2\pi}{L} = 4.4$ rad/m. The maximum detectable wave number is defined by a spatial Nyquist criteria as $k_{max_s} = \dfrac{\pi}{\Delta x} = 68.6$ rad/m.

Making use of the dispersion relation $\omega = ak^2$, where $k = \sqrt{2\pi f/a}$, we find that the temporal sampling parameters correspond to wavenumber limits of $k_{max_t} = 109$ rad/m and $k_{min_t} = 10.9$ rad/m. The total wave number limits are thus $k_{max} = min(k_{max_s}, k_{max_t}) = 68.0$ rad/m, and $k_{min} = max(k_{min_s}, k_{min_t}) = 10.9$ rad/m. Thus, the upper limit on extractable wavenumber (and hence frequency) is determined by the spatial sampling interval Nyquist criterion, and the lower limit on extractable wavenumber is determined by the length of the time record.
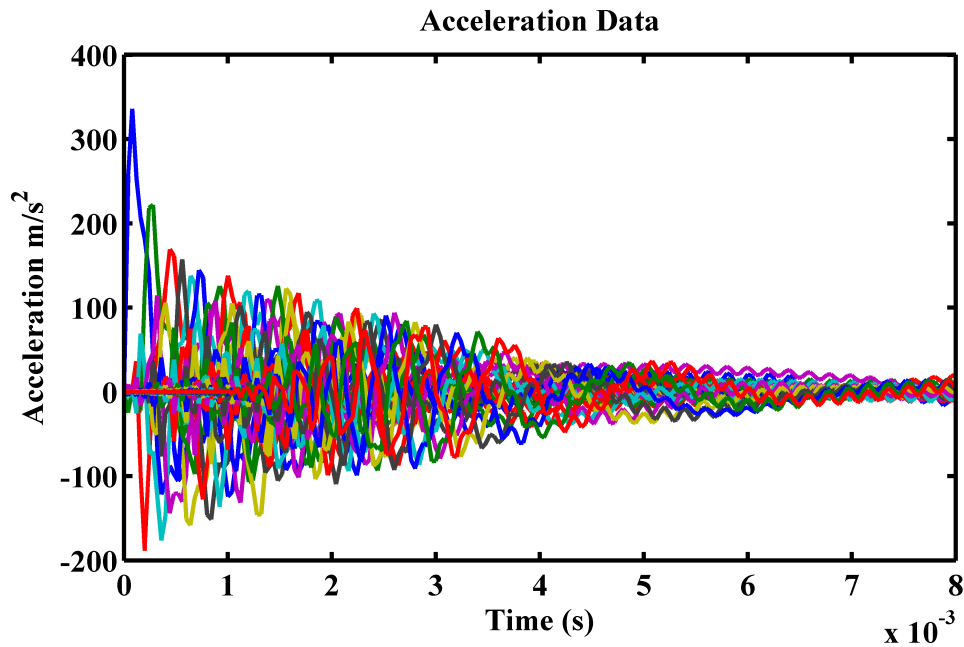
Figure 2.2: Acceleration data for all of the sensors.

18
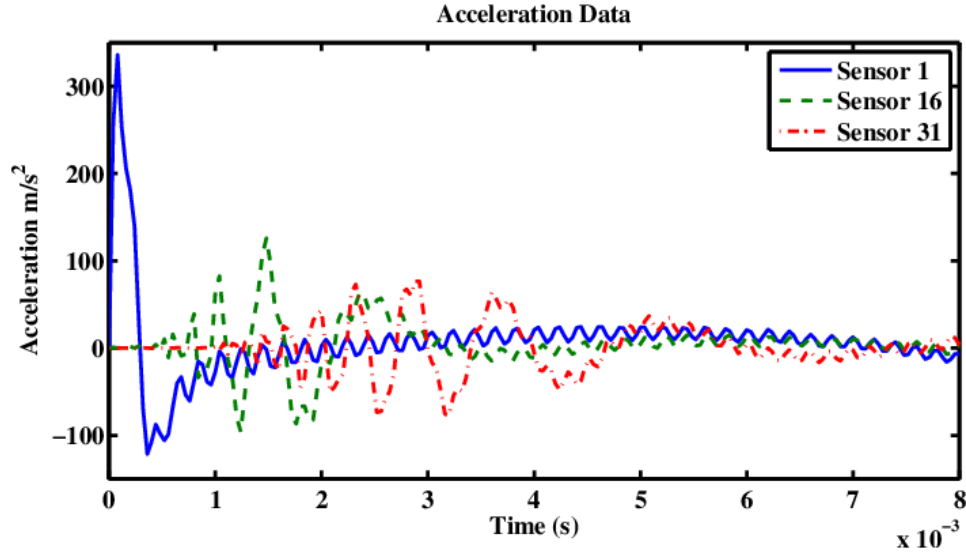
Figure 2.3: Accelerations from sensors 1, 16, and 31.
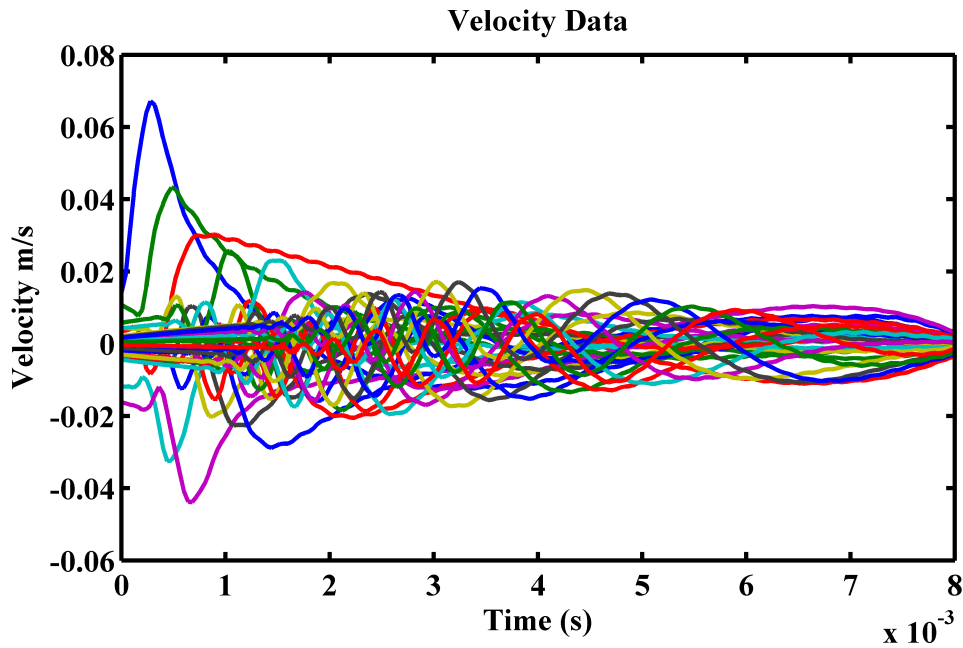
Figure 2.4: Velocity data for all of the sensors.

2.5   Discussion

The acceleration histories shown in . 2.2 show the ensemble signal energy decay as the response propagates into the sand pit, presumably with a small damping effect in the exposed beam as well. Figure 2.3 shows the acceleration history of sensor 1, 16, and 31. The plot

19
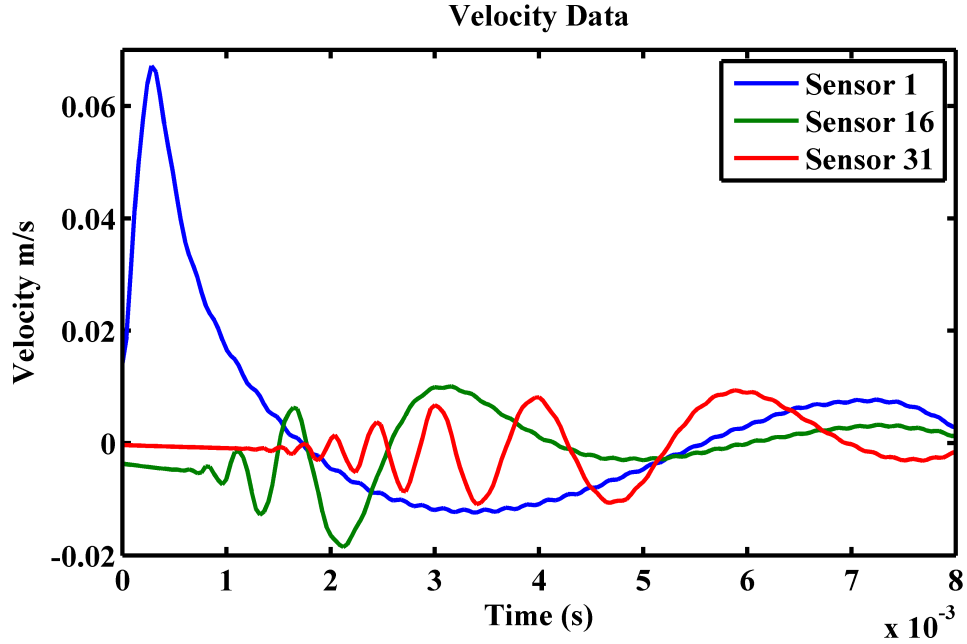
Figure 2.5: Velocities from sensors 1, 16, and 31.
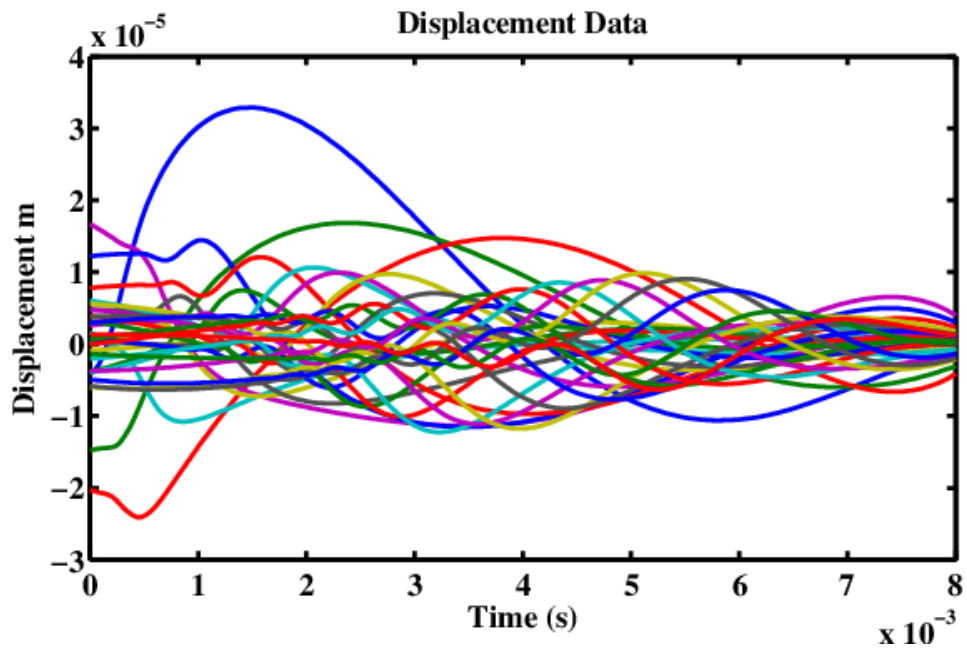
Figure 2.6: Displacement data for all of the sensors.

shows that the wave hits sensor 1 first with a profile that resembles a pulse. The dispersive wave hits sensor 16 next, with high frequencies arriving ahead of the low frequencies, as higher frequencies propagate faster in dispersive beams. The frequencies spread out more
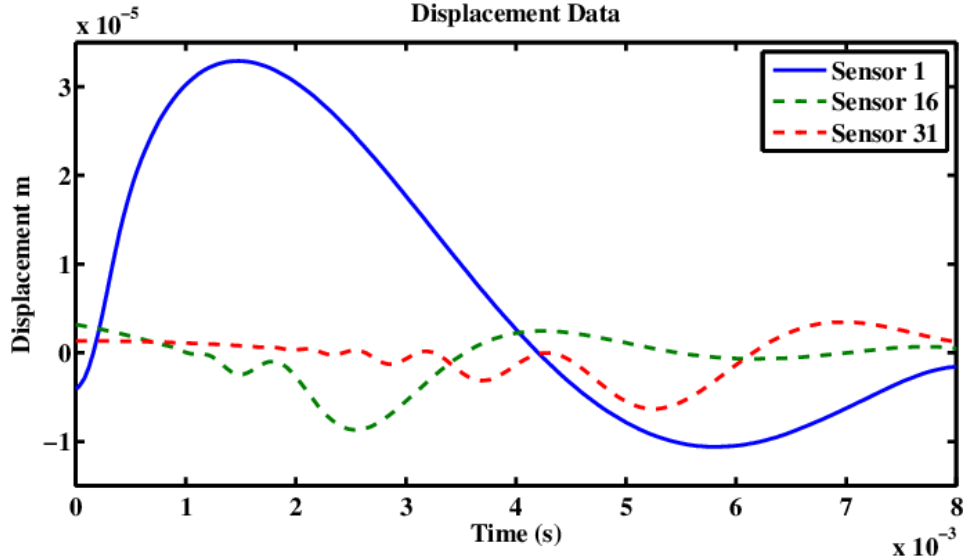
Figure 2.7: Displacements from sensors 1, 16, and 31.

by the time the response reaches sensor 31. The residual high frequency wiggle was due to the pulse reflecting back and forth through the width of the beam and a smaller amplitude can be seen in the velocities plots as well. These trends were also observed by Önsay and Haddow [62]. Various tips were used in the experiment: a metal pointed tip, metal flat tip, and a nylon rounded tip. The both metal tips produced signals with much larger-amplitude residual ringing. The pointed metal tip resulted in the most extreme ring, followed by the flat metal tip. The nylon rounded tip provided the data shown in this paper. The frequency of ringing matched the first mode of vibrations across the height of the beam when viewed as a plate. This was also observed by Önsay and Haddow. Low pass filtering can also have the effect of softer hammer tips.

In reality, the velocity and displacement should start at zero until the wave reaches the sensor location. However, the removal of means, and linear trends using the `"detrend"` command, leaves the velocity and displacement signals with this low-frequency distortion.

21

Distortion of low frequencies outside the range used for the calculation of the dispersion frequencies and wave numbers does not affect the characterization of the dispersion relation in the frequency range of the calculation.

Chapter 3

Complex Orthogonal Decomposition of an Experimental Beam

3.1   Introduction

Complex orthogonal decomposition (COD) [63] is in the family of output-only modal decomposition methods related to proper orthogonal decomposition (POD). POD was first used in mechanics by Lumley to study turbulence in fluid dynamics [14]. Berkooz et al. [17] reviewed the properties of POD for turbulence. POD has been applied to structural dynamics [51–53], and later specifically to extract modal parameters [32, 44, 54, 55]. POD is equivalent to singular value decomposition [16, 55–57], and has several different variations for the extraction of different parameters of interest. These variations include mass-weighted reduced-order proper orthogonal decomposition (MWPOD) [36, 40], Ibrahim time-domain decomposition [58], smooth orthogonal decomposition (SOD) [37, 39, 40], state-variable modal decomposition (SVMD) [40, 59] and, the topic of this paper, COD. To see the connection between POD and COD, next, we will explain POD followed by COD.

First, to perform POD, the analyst captures measurement signals (for example displacements) at different points simultaneously on the structure during its response to some type of

excitation, for example, an impulse [54]. Next, an ensemble matrix, $\mathbf{X} \in \mathbb{R}^{M \times N}$, is created from the sensor measurements, where M is the number of sensors and N is the number of time samples taken. Specifically, $\mathbf{X} = \left[\mathbf{x}_1^T \ \mathbf{x}_2^T \ \cdots \mathbf{x}_M^T\right]^T$, where $\mathbf{x}_i = [x_i(0) \ x_i(\Delta T) \ x_i(2\Delta T) \ \cdots x_i((N-1)\Delta T)]^T$, such that each row of the ensemble matrix is the sampled data from one sensor and each column is a single time sample. Often the mean is subtracted from each sensor signal. Next a correlation matrix, $\mathbf{R} = \dfrac{\mathbf{X}\mathbf{X}^T}{N}$, is computed, such that $\mathbf{R} \in \mathbb{R}^{M \times M}$. Finally, an eigenvalue problem is formulated as $\mathbf{R}\mathbf{v} = \lambda\mathbf{v}$. The eigenvectors are called proper orthogonal modes (POMs). For lightly damped linear vibration systems with a mass matrix proportional to the identity, these converge to linear normal modes [32, 55]. The eigenvalues are called proper orthogonal values (POVs) and relate to modal energy [17, 44]. MWPOD, SOD, SVMD, and COD all involve variations on this algorithm. Each method extracts different modal parameters.

Complex orthogonal decomposition uses simultaneous measurements much like POD. However we must extend these signals into complex analytic form. Such signals do not have negative frequency content, and can be created by manipulation in the frequency domain or by using the Hilbert transform [63, 64]. There are several parameter estimation algorithms that take place in the complex domain, which have been used in the field of electromagnetics, and use response ensembles and eigenvalue problem to estimate parameters, including MUSIC [65] and ESPRIT [66]. The details of the COD algorithm are presented in the next section. Thus far COD has been applied to nematode posturing [67], whiting fish locomotion [45], and discerning traveling and standing modal waves [63]. COD has also been applied to extract the dispersion relation from a simulated beam [46].

In a follow up to the simulated beam study, this paper reports on the application of COD to an experimental beam to extract the geometric dispersion relationship. In the following, Section 3.2 gives a detailed overview of COD. Section 3.3 provides a brief background of waves in an Euler-Bernoulli beam. Section 3.4 describes the experiment and data processing. Section 3.5 shows the results of COD applied to a propagating wave in a beam, with interpretations.

3.2   Complex Orthogonal Decomposition

Complex orthogonal decomposition is an extension of POD with a very similar computation, with the notable exception that COD requires an analytic signal. First, a structure is instrumented, for example with accelerometers distributed evenly on the structure. Next, the structure is excited, in this experiment with an impact hammer, and the sensors are sampled simultaneously. Once the measurement data is acquired the data is arranged in a measurement ensemble $\mathbf{X}$ as described in Section 3.1, and then the analytic form of $\mathbf{X}$ is computed to get $\mathbf{Z}$.

To compute $\mathbf{Z}$, the analytic form of $\mathbf{X}$, first we take the fast Fourier transform (FFT) of each row of $\mathbf{X}$ from the time domain to frequency domain to get $\widetilde{\mathbf{X}}$. The FFT ensemble in the discrete frequency domain can be defined to roughly cover the spectrum from approximately $-\omega_{ny}$ to ω_{ny}, more precisely as indexed from 1 to $N/2$ (for example in the case that N is even). Each row of $\widetilde{\mathbf{X}}$ is the FFT of a sensor signal and each column is a frequency sample, and the elements of $\widetilde{\mathbf{X}}$ are $\widetilde{X}_{ij}$ with $i = 1, \cdots, M$ and $j = -(\frac{N}{2} - 1), \cdots, N/2$. Then the negative spectrum is nullified, and the positive spectrum is doubled, such that the elements

of $\widetilde{Z}_{ij}$ of $\widetilde{\mathbf{Z}}$ are

$$\widetilde{Z}_{ij} = \begin{cases} 0 & \text{if } j < 0 \\ 2\widetilde{X}_{ij} & \text{if } j \geq 0 \end{cases}. \tag{3.1}$$

The complex analytic ensemble is obtained, using the inverse FFT (IFFT), as $\mathbf{Z} = \text{IFFT}(\widetilde{\mathbf{Z}})$.

Now that the measurement ensemble data has been converted into analytic signals the correlation matrix $\mathbf{R}$ is computed as $\mathbf{R} = \dfrac{\mathbf{Z}\mathbf{Z}^{\text{H}}}{N}$, where superscript H denotes the Hermitian operation (conjugate transpose). Once the correlation matrix is computed the eigenvalue problem is formulated such that $\mathbf{R}\mathbf{v} = \lambda\mathbf{v}$. $\mathbf{v}$ is a complex orthogonal mode (COM) and λ is the corresponding complex orthogonal value. Indeed, the correlation matrix can also be formed in the frequency domain as $\widetilde{\mathbf{R}} = \widetilde{\mathbf{Z}}\widetilde{\mathbf{Z}}^{H}/N$, to produce the same COMs [46].

The complex modal coordinate (COC) ensemble, $\mathbf{Q}$, is computed such that $\mathbf{Q} = \mathbf{V}^{-1}\mathbf{Z}$, where each column of $\mathbf{V}$ is an eigenvector $\mathbf{v}$ and $\mathbf{V}^{-1} = \mathbf{V}^{H}$, if normalized, due to orthogonality of the Hermitian eigenvalue problem. Each row $\mathbf{q}_i^T$ of $\mathbf{Q}$ is a sampled COC, such that $\mathbf{Q} = [\mathbf{q}_1 \ \mathbf{q}_2 \ \cdots \ \mathbf{q}_M]^T$, $\mathbf{Q} \in \mathbb{C}^{M \times N}$. For nearly harmonic COCs, the rate of change of the phase with respect to the time sample is equal to the frequency, ω, such that the instantaneous frequency of the i$^{\text{th}}$ modal coordinate is $\underline{\omega}_i = \dfrac{d}{dt}\{\angle\mathbf{q}_i\}$ where, in the sampled case, the time derivative is applied numerically. Similarly, the COMs are complex and the rate of change of the phase of nearly harmonic COMs with respect to the spatial position, x, defines a local wave number of the i$^{\text{th}}$ mode as $\mathbf{k}_i = \dfrac{d}{dx}\{\angle\mathbf{v}_i\}$. Using the COMs and $\mathbf{Q}$, the mean wave number, k_i, and frequency, ω_i, can be extracted for each mode i.

Before applying COD to the beam experiment we review the Euler-Bernoulli beam model.

3.3 Background

3.3.1 Euler-Bernoulli Beam

Applying a traveling wave solution to the Euler-Bernoulli beam equation provides a theoretical framework for the experimental results. The equation of a uniform Euler-Bernoulli beam is

$$\rho A \ddot{y}(x,t) + EI \frac{\partial^4}{\partial x^4}[y(x,t)] = 0, \tag{3.2}$$

where x is the position along the beam, t is time, $y(x,t)$ is the transverse bending displacement, ρ is the mass density, A is the area of beam's cross section, E is the modulus of elasticity, and I is the area moment of inertia of the beam's cross section about the neutral axis. An infinite beam has boundary conditions of bounded displacement and slope.

Following Graff [6], inserting a traveling wave solution in complex harmonic form,

$$y(x,t) = e^{i(kx-\omega t)}, \tag{3.3}$$

into Eq. (3.2), and solving for ω, leads to the geometric dispersion relationship $\omega = ak^2$, where

$$a = \sqrt{\frac{EI}{\rho A}}. \tag{3.4}$$

The phase velocity is then defined as $c = \omega/k = ak$. Thus, for the Euler-Bernoulli beam, the speed of an individually propagating harmonic wave increases linearly with its wavenumber. The group velocity is $c_g = d\omega/dk = 2ak$ for the beam.

In the previous study [46], the COD was applied to a simulated response to an initial Gaussian displacement distribution starting at rest [6]. The extracted traveling wave modes could be related to a form that resembled Eq. (3.3), from which ω and k were extracted as discussed above, and were shown to be consistent with the dispersion relation. This analysis was robust to added sensor noise.

In this work, we apply this analysis to an experiment that emulates a semi-infinite beam with an impulse excitation at the end. Transverse vibrations of a semi-infinite Euler-Bernoulli beam with an end impact have been addressed by Graff [26] by means of Laplace and Fourier transforms, resulting in an analytical expression of the displacement as a function of time. Büssow [68] also treated the problem with slightly different boundary conditions to obtain the displacement in the frequency domain. In the Background Section 3.3.2, we include an analysis to express the displacement and acceleration responses as functions of space and frequency, which can be used when evaluating the response data. We keep in mind that our beam in the sand pit was set up with a focus on extracting the beam's dispersion behavior. Although the constraint of the sand on the beam deflection at large x could cause some deviation between the responses of the ideal theory of [6], [68], and the Background Section 3.3.2, from the experimental beam, even in the unconstrained regions of the beam, we would expect some consistency in some aspects of the response behavior.
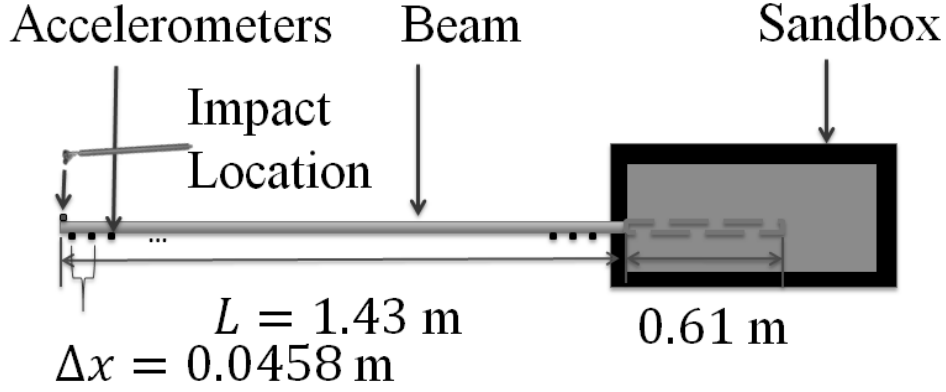
Figure 3.1: Schematic diagram of experimental setup. Top view.

3.3.2 Euler-Beam Solution in the Fourier Domain

The semi-infinite Euler-Bernoulli beam excited with a impulse at $x = 0$ described by $F(0,t) = \hat{F}\delta(t)$ is solved using the Fourier transform. The PDE and boundary conditions (BCs) are listed below:

$$\rho A \ddot{y}(x,t) + EI \frac{\partial^4}{\partial x^4}[y(x,t)] = 0$$

$$y''(0,t) = 0$$

$$y''''(0,t) = \frac{\hat{F}\delta(t)}{EI}$$

$$(3.5)$$

for $x \geq 0$, where the dots indicate partial derivatives with respect to t and the primes indicate partial derivatives with respect to x, and with two additional conditions of bounded displacements and waves that are only allowed to travel in the direction of the positive x-axis.

Taking the Fourier transform of the PDE and BCs yields

$$-\omega^2 \widetilde{Y}(x,\omega) + \alpha^4 \widetilde{Y}''''(x,\omega) = 0$$

$$\widetilde{Y}''(0,\omega) = 0$$

$$\widetilde{Y}(0,\omega) = \frac{\hat{F}}{EI}$$

where $\alpha^4 = \frac{EI}{\rho A}$, while remembering the bounded displacements and one-directional wave condition. Now we have an ODE of the form

$$\widetilde{Y}'''' - \beta \widetilde{Y} = 0$$

where $\beta = \frac{\omega^2}{\alpha^4}$. Substituting in the standard trial solution $\widetilde{Y} = e^{rx}$ and solving for r yields

$$r = \pm \frac{\omega^{1/2}}{\alpha}, \pm \frac{i\omega^{1/2}}{\alpha},$$

which leads to

$$\widetilde{Y}(x,\omega) = A_1 e^{\frac{\sqrt{\omega}}{\alpha}x} + A_2 e^{-\frac{\sqrt{\omega}}{\alpha}x} + A_3 e^{i\frac{\sqrt{\omega}}{\alpha}x} + A_4 e^{-i\frac{\sqrt{\omega}}{\alpha}x}.$$

Since the displacements are bounded, $A_1 = 0$, and since waves can only travel in the positive x direction, $A_3 = 0$, which can be seen by considering that the inverse Fourier transform combines these terms with $e^{i\omega x}$. Applying the other two boundary conditions, $A_2 = A_4$ are

30

determined, resulting in

$$\widetilde{Y}(x,\omega) = \frac{\hat{F}}{\sqrt[4]{EI}(\rho A)^{3/4}\,\omega^{3/2}(i-1)}(e^{-\frac{\sqrt{\omega}}{\alpha}x} + e^{-i\frac{\sqrt{\omega}}{\alpha}x}). \qquad (3.6)$$

This provides the frequency domain description of the displacement response. A loosely described derivation can be found in [68].

The acceleration response in the frequency domain is thus

$$\widetilde{A}(x,\omega) = \frac{-\omega^2\hat{F}}{\sqrt[4]{EI}(\rho A)^{3/4}\,\omega^{3/2}(i-1)}(e^{-\frac{\sqrt{\omega}}{\alpha}x} + e^{-i\frac{\sqrt{\omega}}{\alpha}x}). \qquad (3.7)$$

3.4 Experiment

3.4.1 Setup

The test specimen was a rectangular steel beam with a constant cross section. In effort to emulate a semi-infinite free beam, the beam was suspended with elastic cords, such that one end was free, and the other was embedded in a sand pit, as done by Önsay and Haddow [62]. The sand absorbs the wave and prevents reflections off the buried end of the beam. A schematic of the experiment is shown in Figure 3.1. In this case, the sandbox was filled with unpacked coarse sand. The beam had a 0.0045 m × 0.0698 m cross section. The length of the beam was 2.04 m. The unburied part of the beam measured 1.43 m, such that approximately 0.609 m was buried in the sand. The density and modulus of elasticity of the beam were 7870 kg/m^3 and 200 GPa, respectively, based on published values for steel. From the geometry and material properties the theoretical value from Eq. (3.4) is $a = 6.548$ m^2/s.

The beam was sensed with 31 accelerometers placed at a distance $\Delta x = 0.0458$ m apart over a distance of $L = 1.4198$ m and was sampled at $f = 25,000$ Hz using a National Instrument's PXI data acquisition system. The beam was struck with a PCB model 086C80 mini impact hammer, lightly such that bending deflections were not visible to the naked eye.

3.4.2   Data Processing

The data included 100 samples before the hammer impact and 300 samples after the impact for a total of 400 samples. We aim to integrate the acceleration data to obtain velocity and displacement. Numerical integration can be problematic because an integration constant is introduced, and low-frequency noise is amplified and can cause the integrated signal to drift. To reduce these effects the following steps were taken. First the data was filtered forward and backward with a high-pass filter with a cutoff frequency of 100 Hz. Second, the mean of each sensor's time history was subtracted from its samples using Matlab's `"detrend"` with a `"constant"` modifier. Third, any linear trends were removed using the same command as above with a `"linear"` modifier. Fourth, the signals were translated on the time axis such that the sample before the hammer impact had a time and force value of zero. The first and last 100 samples were truncated leaving the start of the impact plus 200 samples.

Next, to get velocities, the signals were numerically integrated using the `"cumtrapz"` command. The means were subtracted from the velocities, which were then high pass filtered, and integrated once more to get displacements. The means were subtracted from displacements and the displacements were filtered for a final time. These $N = 200$ samples of displacements were then used for COD.

The minimum detectable wavenumber defined by the span of sensors, L, is $k_{min_s} = \dfrac{2\pi}{L} =$ 4.4 rad/m. The maximum detectable wavenumber is defined by a spatial Nyquist criterion as $k_{max_s} = \dfrac{\pi}{\Delta x} = 68.6$ rad/m. Based on the sampling rate $f = 25,000$ Hz and time record of $N/f = 0.008$ s, the maximum detectable frequency is $f_{max_t} = 12,500$ Hz and the minimum detectable frequency is $f_{min_t} = 125$ Hz.

Making use of the theoretical dispersion relation $\omega = ak^2$, or $k = \sqrt{2\pi f/a}$, we find that the temporal sampling parameters correspond to theoretical wavenumber limits of $k_{max_t} = 109$ rad/m and $k_{min_t} = 10.9$ rad/m. The approximate total wavenumber limits are thus $k_{max} = min(k_{max_s}, k_{max_t}) = 68.6$ rad/m, and $k_{min} = max(k_{min_s}, k_{min_t}) = 10.9$ rad/m. Thus, the upper limit on extractable wavenumbers (and hence frequencies) is determined by the spatial sampling interval Nyquist criterion, and the lower limit on extractable wavenumbers is determined by the length of the time record.

3.5   Results and Discussions

The acceleration histories in Figure 3.2 show the ensemble signal energy decay as the response propagates into the sand pit, presumably with a small damping effect in the exposed beam as well. Figure 3.3 shows the acceleration history of sensors 1, 16, and 31. The plot shows that the wave hits sensor 1 first with a profile that resembles a pulse. The dispersive wave hits sensor 16 next, with high frequencies arriving ahead of the low frequencies, as higher frequencies propagate faster in dispersive beams. The frequencies spread out more by the time the response reaches sensor 31. The residual high frequency wiggle is due to the pulse reflecting back and forth through the width of the beam. These trends were also observed
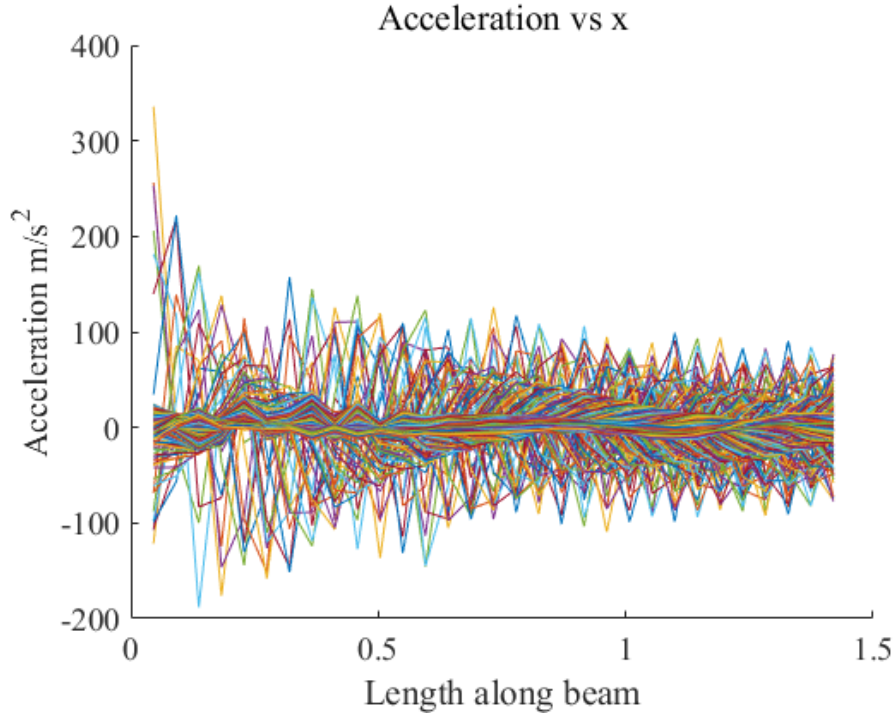
Figure 3.2: Acceleration data vs position along the beam

by Önsay and Haddow [62].

Various tips were used in the experiment: a metal pointed tip, metal flat tip, and a nylon rounded tip. The metal tips excited higher frequencies and thus produced signals with much larger-amplitude residual ringing through the beam width. The pointed metal tip resulted in the most extreme ring, followed by the flat metal tip. Our interest is in extracting behavior predicted by the one-dimensional beam model, and hence we used a softer tip. The nylon rounded tip generated the data shown in this thesis, and some ringing was still excited. The frequency of ringing matched the first mode of vibrations across the height of the beam, when viewed as a plate. Low pass filtering can also have the effect of softer hammer tips.

The accelerations were filtered and integrated twice, according to the process of Section 3.4.2,
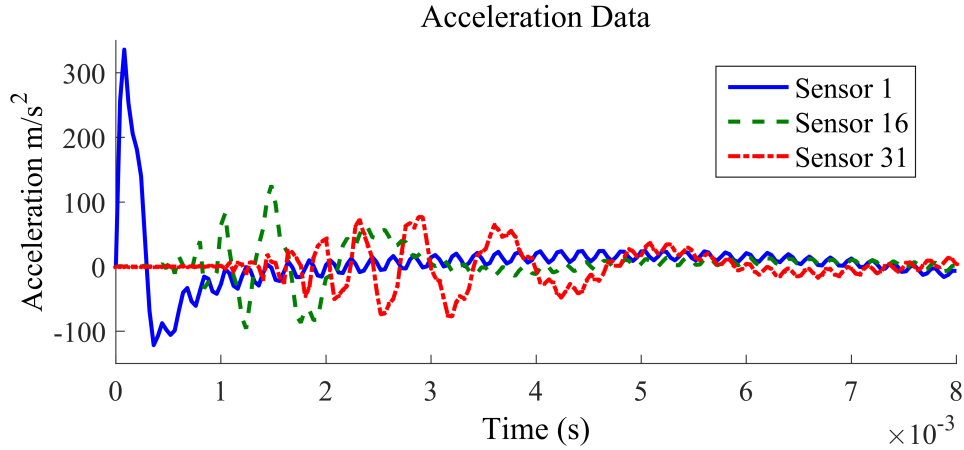
Figure 3.3: Accelerations from sensors 1,16, and 31
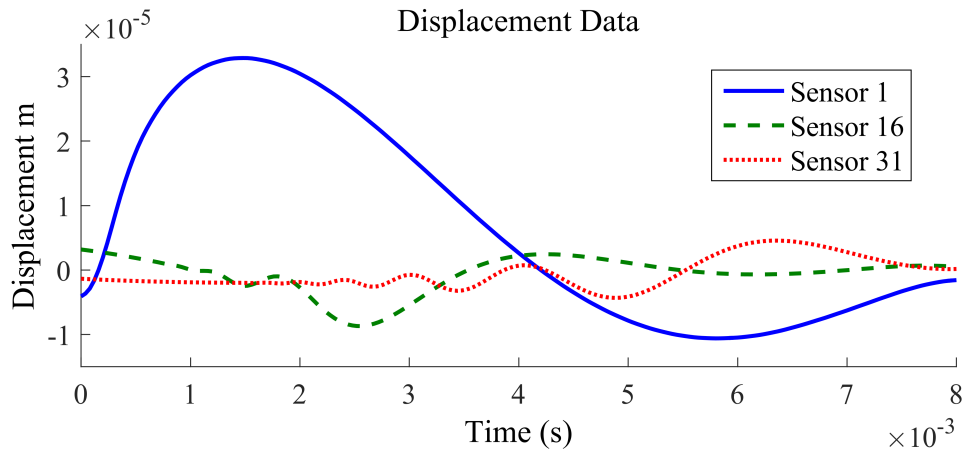
Figure 3.4: Displacements from sensors 1, 16, and 31

to produce the displacements in Figure 3.4, where sensors 1, 16, and 31, only, are shown for clarity. In reality, the displacement should start at zero until the wave reaches the sensor location. However, despite the high-pass filtering and removal of means and linear trends together, the signals were left with some low-frequency distortion. This distortion, however, is outside of the frequency range used for the calculation of the dispersion frequencies and wavenumbers, and therefore does not affect the modal dynamics nor the characterization of dispersion within this range of calculation. Nonetheless, we can see some key features in Figure 3.3 carrying over to Figure 3.4, showing the high frequency components of wave
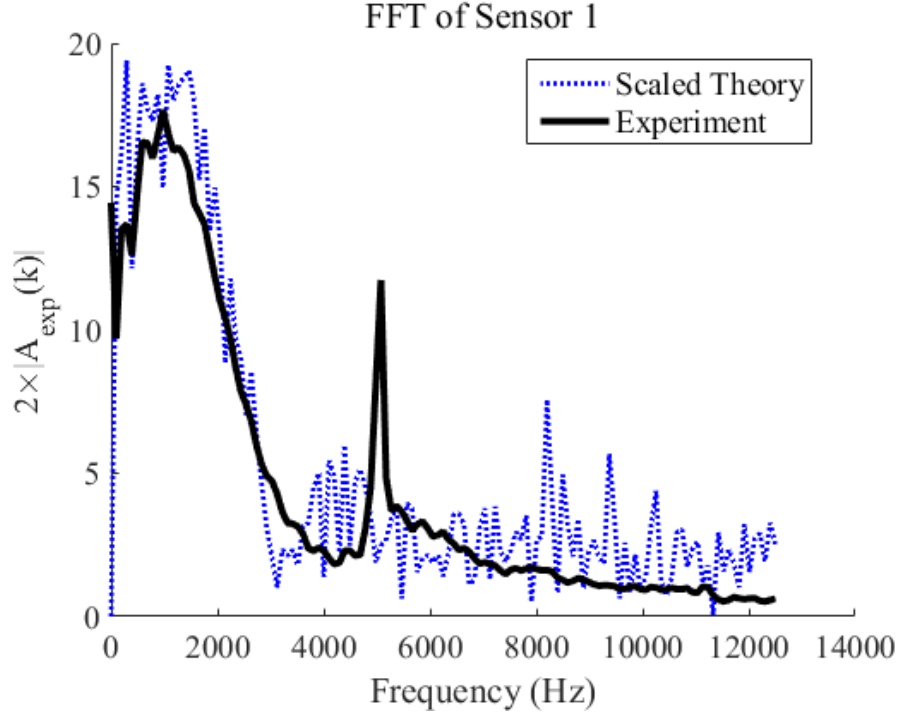
Figure 3.5: Sensor 1

displacement arriving in sensors 16 and 31 ahead of lower-frequency components, consistent with beam dispersion.

Black (dark) solid lines in Figs. 3.5 - 3.7 show the FFTs of accelerometers signals for sensors 1, 16, and 31. The dotted lines show the scaled theoretical accelerations. Figure 3.8 shows the FFT of the impact hammer signal. We can compare the responses with the theoretical predictions. If we consider that the response of Eqn. (3.2) under an end impact loading is $\tilde{Y}(x,\omega)$ as given in Eqn. (3.6) in the background Section 3.3.2, then $\tilde{H}(x,\omega) = \tilde{Y}(x,\omega)/\hat{F}$ can be considered as a unit impulse response function in the frequency domain, that is, a frequency response function between the displacement $y(x,t)$ and the end input, such that for the case of an ideal impulse at the endpoint, where $\tilde{F}(\omega) = \hat{F}$, then $\tilde{Y}(x,\omega)$ results in the Eqn. (3.6). However, Figure 3.8 shows that the
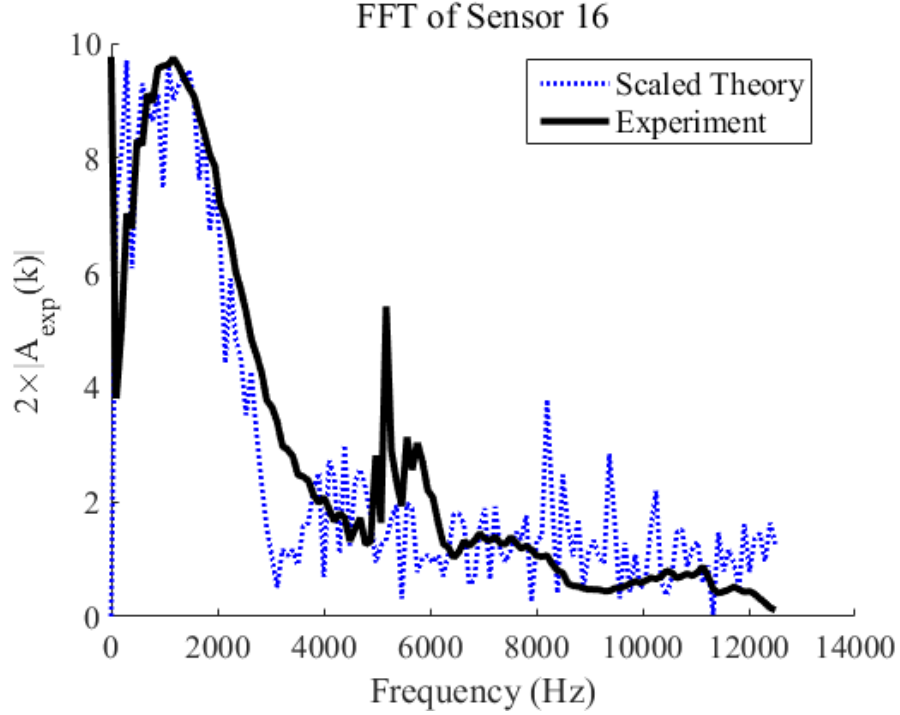
Figure 3.6: Sensor 16

impact is not ideal, and the associated input $\bar{F}(\omega)$ is confined to a finite bandwidth. The response to this nonideal impact is $\bar{Y}(x,\omega) = \tilde{H}(x,\omega)\bar{F}(\omega)$. The acceleration response is likewise $\bar{A}(x,\omega) = \tilde{A}(x,\omega)\bar{F}(\omega)/\hat{F}$, where $\tilde{A}(x,\omega)$ is given as Eqn. (3.7) in the background Section 3.3.2.

We have evaluated $|\tilde{A}(x,\omega)|$ at the sensor locations x_i, and at the frequencies of the FFT, and then obtained $|\hat{A}(x_i,\omega)| = |\tilde{A}(x_i,\omega)||\bar{F}(\omega)|/\hat{F}$ with a normalized input signal ("normalized" to optimize the accuracy for sensor 16). The results are the dotted lines in the plots of Figures 3.5 - 3.7. Thus, relative to the normalized input, the results are in good qualitative agreement. The magnitude of the plot for sensor 1 is very sensitive, as the theory predicts a very steep change in response amplitude as x gets small. These plots show that, although the beam is embedded in a sand pit down stream of the wave, the exposed region of
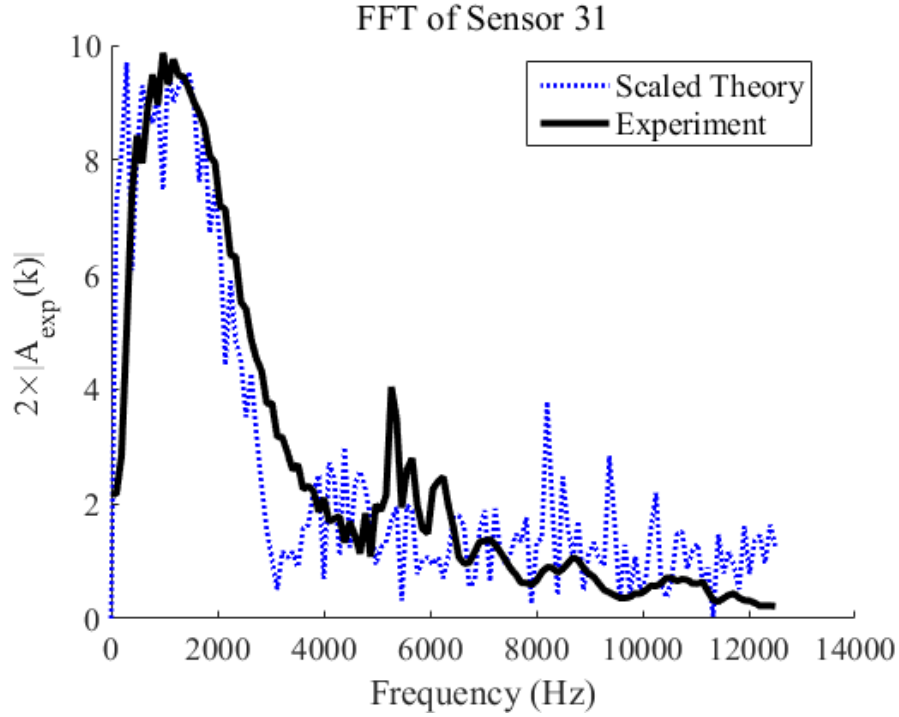
Figure 3.7: Sensor 31

the beam behaves, in the bandwidth of our excitation, similarly as a if it were a semi-infinite beam. It also shows that the analysis of the Euler-Bernoulli beam under an end impact provides useful predictions of behavior in the frequency and space domains, particularly if the input is quantified.

COD was applied, and some of the COMs (Figure. 3.9) and COCs (Figure 3.10) are shown for illustration purposes. The COMs depicted in Figure 3.9 show the real and imaginary parts of selected extracted complex modes, normalized such that each modal vector has unit amplitude. The plots are parameterized in the sensor location index. Thus, there are 31 real and imaginary ordered pairs plotted and connected with straight lines. A perfect whirl would indicate a purely spatially harmonic wave mode whose real and imaginary parts are 90 degrees out of phase. Thus, the spatially whirling extracted modes resemble harmonic
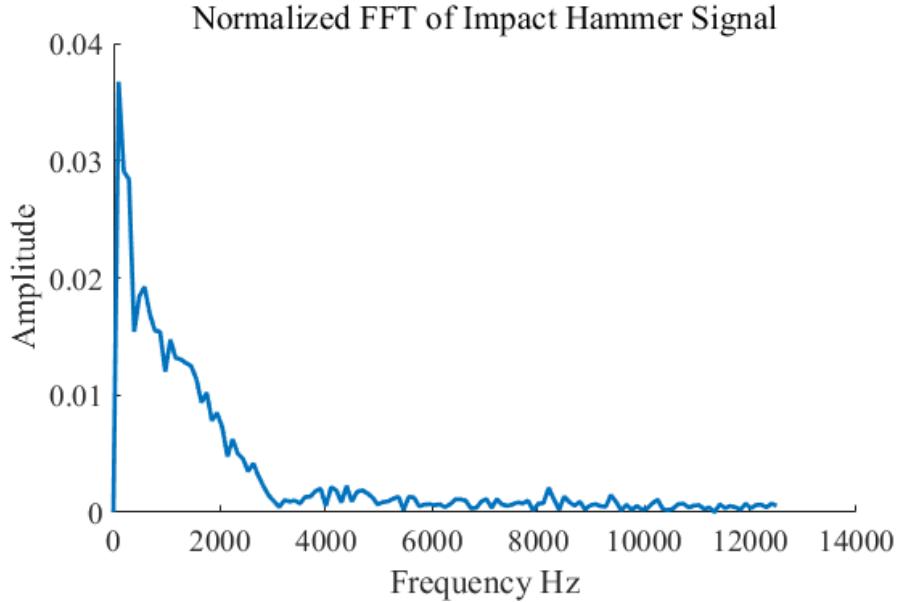
Figure 3.8: FFT of the modal impact hammer signal.

wave modes, and the spatial whirling rate can then be used to estimate the complex modal wave number, as long as the spatial sampling interval is small enough to accurately estimate a wavenumber.

The COCs plotted in Figure 3.10 show the real and imaginary parts of corresponding complex modal coordinates. The normalization of the complex modes, and the COC modal energy (the COVs), define the amplitude of the complex modal coordinates. These plots are parameterized in the time index. Thus, there are 200 points plotted in each graph, connected with lines, such that the graphs appear rather smooth for the lower frequency modes. In this time parameterization, the typical trend is that the modal coordinate begins as a nearly harmonic oscillation, and then decays as the modal component travels off of the measurement zone. Examples of the real parts as functions of time are shown in Figs. 3.11 and 3.12. Since the higher frequencies travel faster through the beam, the higher frequency modal coordinates have shorter durations of nearly harmonic oscillation. This trend was also observed in decompositions of numerically simulated waves [46]. In the experiment, the

39
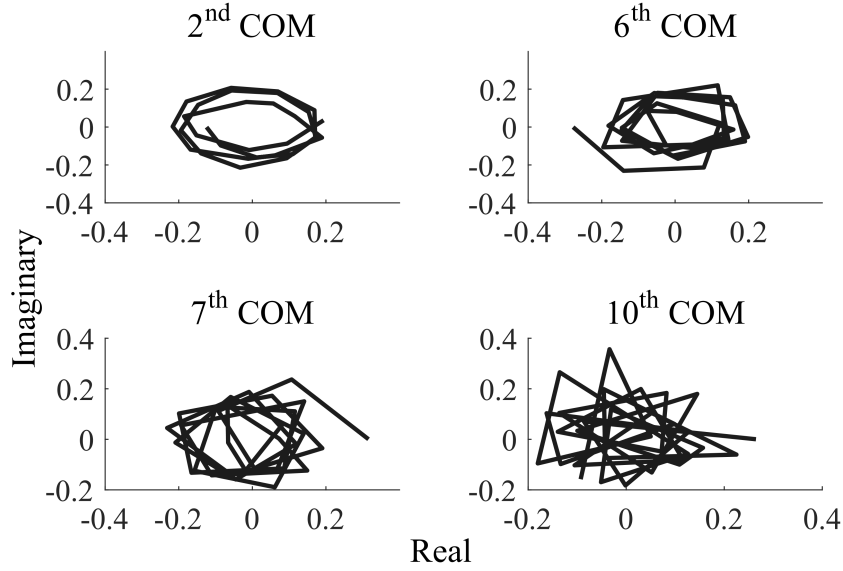
Figure 3.9: Selected COMs. Top left: 2nd modal COM. Top right: 6th COM which is less circular than second. This trends continues and is illustrated in the lower left: 7th COM. Lower right: 10th COM.

modes are not pure harmonics, and there is noise and modeling error that contribute to some modal pollution apparent as a lower amplitude, lower frequency oscillation after the strong harmonic has left the measurement zone. The interval of the strong nearly harmonic oscillation is then used to extract the modal coordinate temporal whirl rate, which represents the frequency of the mode. The mechanism for how experimental error leads to modal pollution was analyzed previously [67].

The extracted geometric dispersion relationship is shown in Figure 3.13. In this figure, values of ω and k are plotted in the ranges for which the mode shapes and modal coordinates exhibited intervals of well defined whirls.

In Figure 3.13 it can be seen that the experimental data show good agreement with theory. From theory we have $\omega = ak^2$ where $a = 6.548$ m^2/s. A least squares (LSQ) fit
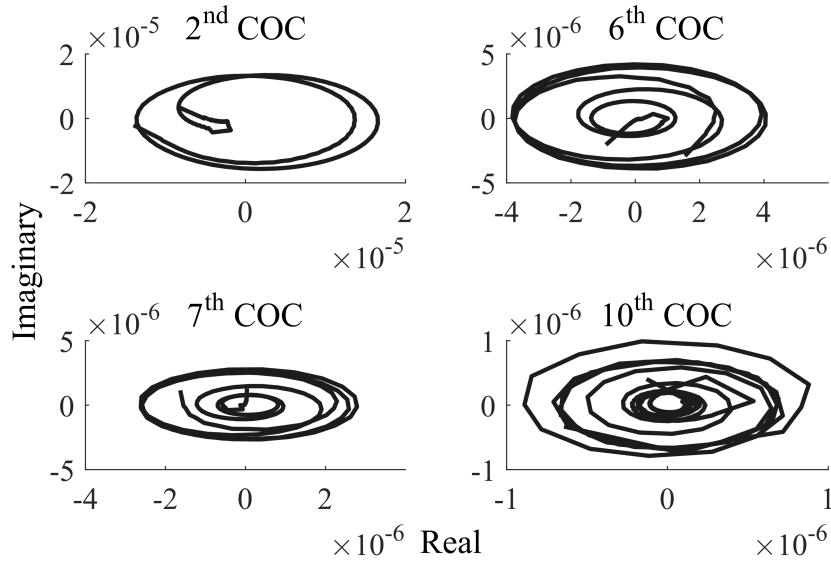
Figure 3.10: Selected COCs. Top left: 2nd modal COC. Top right: 6th COC which shows attenuation after some initial oscillations. This trends continues and is illustrated in the lower left: 7th COC. Lower right: 10th COC

of the the geometric dispersion relation using COD extracted k and ω leads to a value of $a_{fit} = 6.4431$ m^2/s, which gives an underestimation of 1.61%. Based on regression error analysis [69], the extracted valued of 6.44 m^2/s leads to a mean squared error of 6.1667×10^4 rad/s, and its 95% confidence interval is $a = [6.2638, 6.26224]$ m^2/s. When the data processing laid out in Section 3.4.2 was done without the high-pass filtering, i.e. where the data just had the means subtracted followed by integration repeated as needed to get displacements, the least squares estimate of a was $a_{fit} = 6.8$ m^2/s, which was an overestimation of 3.8%.

The phase velocity is shown in Figure 3.14, comparing the equation $c = ak$ with $c = \omega/k$ computed from COD-extracted ω and k. The solid line is theory and the circles are COD extracted data points. Similarly, the group velocity is shown in Figure 3.15, from values that were computed using forward differences on the COD extracted ω and k from Figure 3.13.
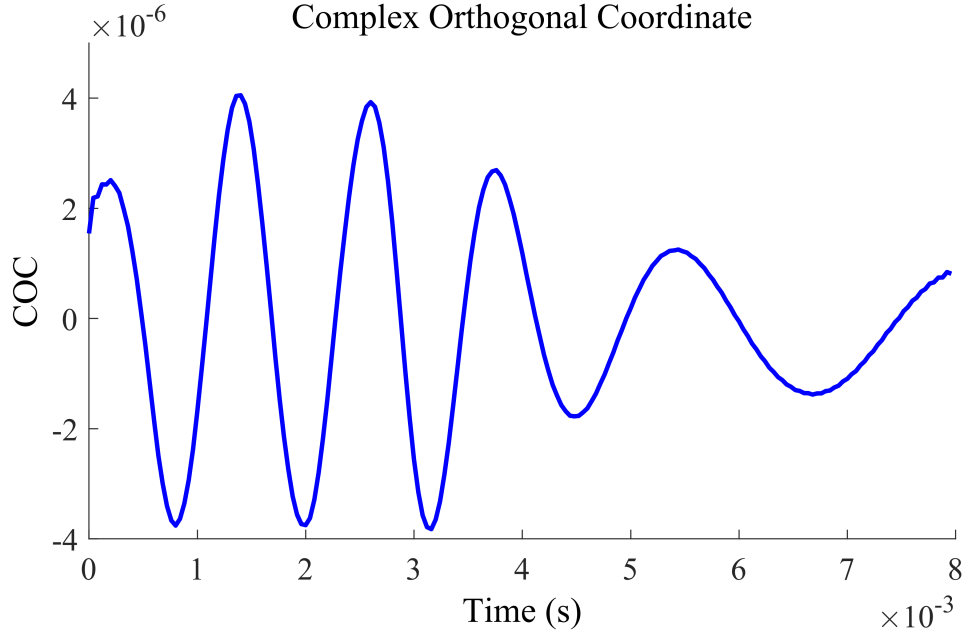
Figure 3.11: Real part of complex orthogonal coordinate number 4.

Several things are worth noting at this point. We find that the COVs increase with decreasing modal wavenumber (decreasing frequency). This may be sensible if we consider that the impulse excitation is slightly stronger for lower frequencies (see Figure 3.8). Furthermore, the higher frequencies propagate faster according to the beam theory, such that lower frequency modes are active in the measurement zone for longer time intervals. The excitation bandwidth and modal activity duration contribute to higher mean squared amplitudes (COVs) for lower modes.

We also see that the extracted data in Figure 3.13 falls within the theoretical limits of k_{min}, k_{max}, and ω_{max} determined by sampling parameters. Spatial resolution has a great effect: approximately the lowest 1/3 of the COMs (those with highest COVs and lower wavenumbers) have good whirl properties with high enough spatial sampling resolution to
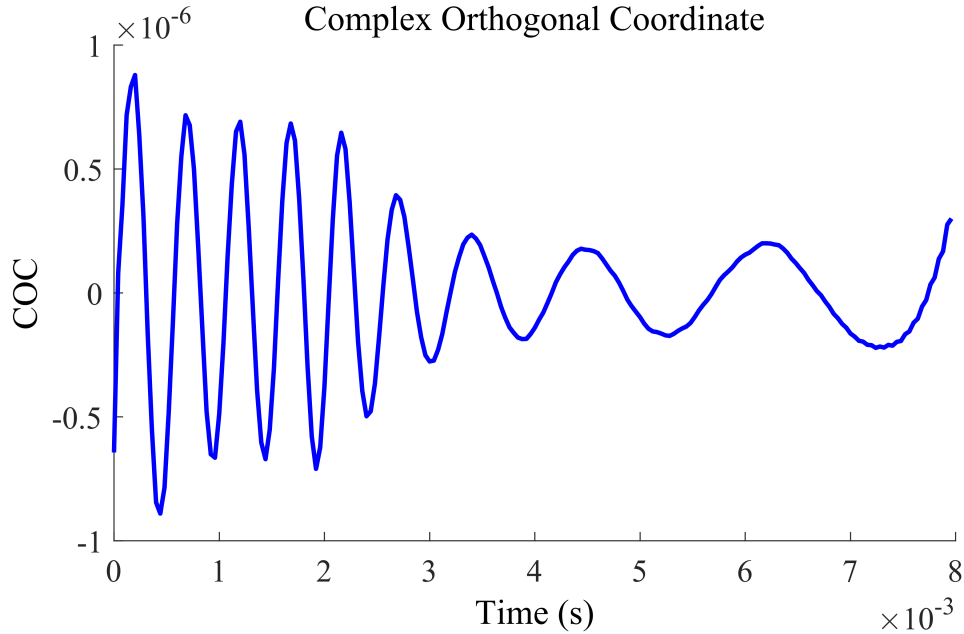
Figure 3.12: Real part of complex orthogonal coordinate number 8.

allow for good k extraction. The second COM shown in Figure 3.9 had the best circular whirling. As the COVs decrease the COMs become less circular in the complex plane. This is partly because the spatial resolution becomes coarse as the modal wave number increases. However the COCs are effected to a lesser degree by resolution limitations than the COMs, which makes sense because the spatial sampling distance and time record were found to be the parameters that limited the accessible frequency range, and the temporal sampling was thus abundantly fast, such that the accessible modal coordinates were smoothly sampled.

3.5.1 Using COCs to Extract Modal Amplitudes

It may be of interest to determine the amplitude of the wave traveling through the beam as a function of frequency. To achieve this the fast Fourier transform (FFT) of the the COCs were computed and the maximum magnitude and its frequency was recorded to derive COD
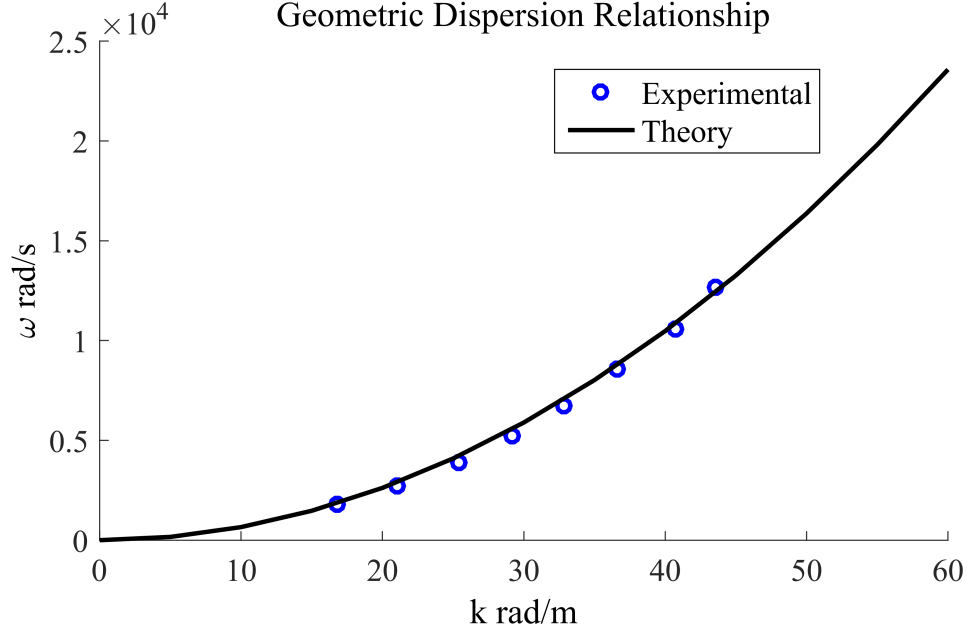
Figure 3.13: Experimental results. Theoretical dispersion relationship for the Euler-Bernoulli beam (Solid line). COD extracted data points ($\circ$).

extracted $|\widetilde{A}_{cod}(x,\omega)|$ shown as the red circles in Figure 3.16. In order to compare this with

theory, $\widetilde{A}(x,\omega)$ was computed for each sensor location i and then each $\widetilde{A}(x_i,\omega)$ was multiplied

by the FFT of the modal impact hammer signal shown in Figure 3.8 to get $\bar{A}(x_i,\omega)$ where

$i = 1, \cdots, 31$. A composite was created such that $U(\omega) = \dfrac{\sum \bar{A}(x_i,\omega)}{M}$ was computed and is

shown as the solid line in Figure 3.16. $U(\omega)$ is simply the average of the scaled theoretical

acceleration for each sensor. The plot of the $\widetilde{A}_{cod}(x,\omega)$ (circles) and $U(\omega)$ (line) is shown in

Figure 3.16 and shows great agreement.

3.6   Conclusion

Experiments were performed on a thin beam suspended in the sand to emulate a semi-infinite

beam. The beam was instrumented with accelerometers, excited with an impulse, and

the measured responses were integrated into displacement signals and then analyzed using
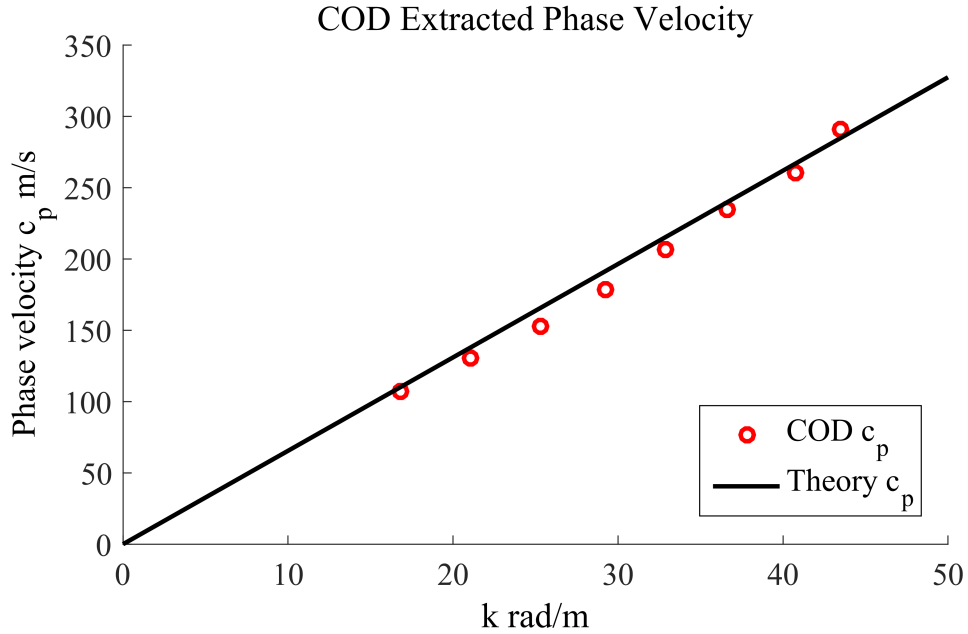
Figure 3.14: Phase velocity

COD to extract the underlying complex modes. True to beam theory, higher frequency wave components traveled faster, and thus remained active for shorter segments of the time record, than lower frequency components. The measured acceleration responses also agreed qualitatively with theoretical responses to the measured input pulse.

The lower-frequency extracted complex modes resembled harmonic complex waveforms. The associated modal coordinates were dominantly harmonic during a time interval dictated by the wave speed of the corresponding component of the wave form, and the length of the measurement zone on the beam. The nearly harmonic nature of the decomposed mode shapes and modal coordinates contained information on modal wavenumber and frequencies, which could be estimated.

With this approach, we extracted the dispersion characteristics over a frequency and

45
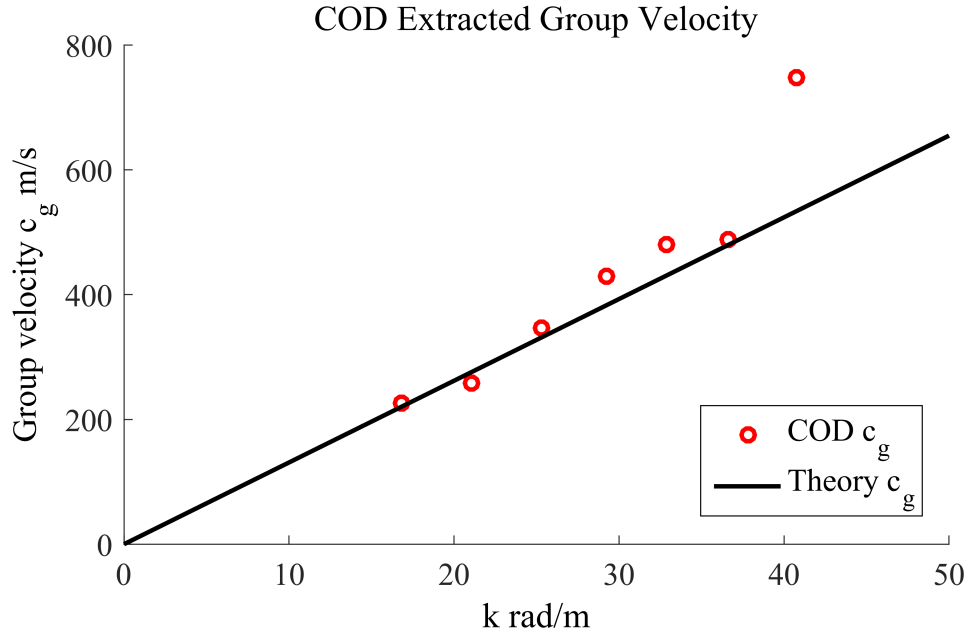
Figure 3.15: Group velocity

wavenumber interval, as well as the amplitude of the waves traveling through the beam. The results were consistent with Euler-Bernoulli beam theory, and with a previous analysis of simulated response data.

The work shows that COD is a fast and simple tool that can be used to extract the geometric dispersion relationship between the frequency, phase velocity, or group velocity, the wave number, and wave amplitudes for waves traveling in a semi-infinite uniform structure.
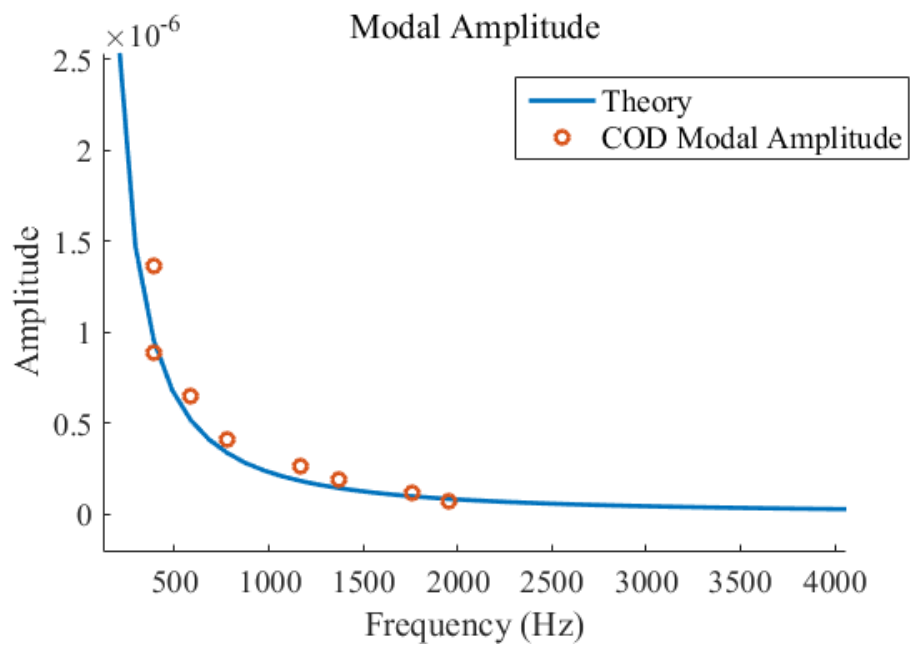
Figure 3.16: COD extracted modal amplitude vs frequency (∘) compared to theory

Chapter 4

Smooth Complex Orthogonal Decomposition in the Time Domain

4.1 Introduction

During the middle of the 20th century various researchers independently developed proper orthogonal decomposition (POD) [14,17,70,71] which was applied to statistics and turbulent fluid flows. POD later caught the interest of structural engineers and was used to extract mode shapes from vibrating structures [58, 72–74]. Other generalizations of POD were developed, such as the smooth orthogonal decomposition (SOD) for finding the natural frequencies and linear normal modes [37, 39], and the state variable modal decomposition (SVMD) [59] for finding natural frequencies, normal modes, and (in theory) modal damping.

Soon after POD was expanded for extracting traveling wave modes using complex orthogonal decomposition [63]. Complex orthogonal decomposition (COD) [46] can extract nonsynchronous and standing waves of vibrating structures, and when waves are traveling through an elastic medium COD can be used to extract the wavenumbers, frequencies, and the dispersion

relationship of the waves. In the application of COD the wavenumber is extracted from the eigenvector, and the frequency is extracted from the modal coordinate.

A new generalization of COD and SOD is outlined here called the smooth complex orthogonal decomposition (SCOD). It will be shown that with SCOD the wavenumber and frequency can be extracted from the eigenvector and eigenvalue of the SCOD eigenvalue problem (EVP). A mathematical development for SCOD will be covered in Section 4.2. SCOD will be applied to a simulated infinite beam in Section 4.4, and experimentally to a rectangular beam in Section 4.4.2. A primer for SOD is reviewed in the following subsection.

4.1.1 Primer of Smooth Orthogonal Decomposition

We will start by relating SOD [37] to the symmetric effective mass-spring system, following [39]. Given the general undamped linear free vibration mass-spring equation

$$\mathbf{M}\ddot{\mathbf{x}} + \mathbf{K}\mathbf{x} = 0 \tag{4.1}$$

and substituting in the assumed solution of $\mathbf{x} = \underline{\phi}e^{i\omega t}$ leads to the generalize eigenvalue problem in the form of

$$\lambda \mathbf{M}\underline{\phi} = \mathbf{K}\underline{\phi}, \tag{4.2}$$

where the eigenvalues $\lambda = \omega^2$ are modal frequencies squared, and the eigenvectors $\underline{\phi}$ are the mode shapes. In matrix form, we can write

$$\mathbf{M}\mathbf{\Phi}\mathbf{\Lambda} = \mathbf{K}\mathbf{\Phi}, \tag{4.3}$$

49

where $\mathbf{\Phi}$ is a matrix consisting of columns $\underline{\phi}_i$ and $\mathbf{\Lambda}$ is a diagonal matrix whose elements are ω_i^2. We will show the relationship between the mass-spring system and the smooth orthogonal decomposition.

SOD is defined by

$$\lambda \mathbf{R} \underline{\psi} = \mathbf{S} \underline{\psi}, \tag{4.4}$$

or in matrix form,

$$\mathbf{R} \mathbf{\Psi} \mathbf{\Lambda} = \mathbf{S} \mathbf{\Psi}, \tag{4.5}$$

where λ is a smooth orthogonal value (SOV), which will be seen to approximate the modal frequency squared, $\mathbf{\Lambda}$ is a diagonal matrix whose elements are the λ_i, $\underline{\psi}$ is the smooth orthogonal mode, and $\mathbf{\Psi}$ is a matrix consisting of columns $\underline{\psi}_i$. SOD involves two correlation matrices, $\mathbf{R}$ and $\mathbf{S}$, where

$$\mathbf{R} = \frac{\mathbf{X} \mathbf{X}^T}{N} \tag{4.6a}$$

$$\mathbf{S} = \frac{\mathbf{V} \mathbf{V}^T}{N}, \tag{4.6b}$$

and where $\mathbf{X}$ is a measurement ensemble of displacements, and $\mathbf{V}$ is a measurement ensemble of velocities. Typically the mean of the time history of each sensor is subtracted from each of the data samples of that sensor. The general form of all ensembles used in this body of

work is, for the example of the displacements,

$$\mathbf{X} = \begin{bmatrix} x_1(0) & x_1(\Delta t) & \cdots & x_1((N-1)\Delta t) \\ x_2(0) & x_2(\Delta t) & \cdots & x_2((N-1)\Delta t) \\ \vdots & \vdots & \ddots & \vdots \\ x_M(0) & x_M(\Delta t) & \cdots & x_M((N-1)\Delta t) \end{bmatrix} \tag{4.7}$$

where M is the number of sensors and N is the number of samples. The time history for each sensor is organized in rows, such that each column is a set of samples at each sampling interval.

Starting with the SOD eigenvalue problem, as

$$\mathbf{R}\mathbf{\Psi}\mathbf{\Lambda} = \mathbf{S}\mathbf{\Psi}$$

and substituting in the expressions for $\mathbf{R}$ and $\mathbf{S}$, leads to

$$\mathbf{X}\mathbf{X}^T\mathbf{\Psi}\mathbf{\Lambda} = \mathbf{V}\mathbf{V}^T\mathbf{\Psi}$$

Chedize and Zhou [37] used the approximation $\mathbf{V} \cong \mathbf{X}\mathbf{D}^T$, and showed that $\mathbf{X}\mathbf{D}\mathbf{D}^T\mathbf{X}^T \cong -\mathbf{X}\mathbf{A}^T$, where $\mathbf{D}$ is a matrix that performs a simple finite difference numerical derivative. Hence, $\mathbf{S} = \mathbf{V}\mathbf{V}^T \approx -\mathbf{X}\mathbf{A}^T$. Hence, $N\mathbf{S} = \mathbf{V}\mathbf{V}^T \approx -\mathbf{X}\mathbf{A}^T$. Plugging this into $\mathbf{S}$, the EVP becomes

$$\mathbf{X}\mathbf{X}^T\mathbf{\Psi}\mathbf{\Lambda} = -\mathbf{X}\mathbf{A}^T\mathbf{\Psi}.$$

Now noting that $\mathbf{A}$ is an ensemble of accelerations, then from $\mathbf{MA} + \mathbf{KX} = \mathbf{0}$, we have $\mathbf{A} = -\mathbf{M}^{-1}\mathbf{KX}$. Then

$$\mathbf{XX}^T\boldsymbol{\Psi}\boldsymbol{\Lambda} = \mathbf{X}[\mathbf{M}^{-1}\mathbf{K}^T\mathbf{X}]^T\boldsymbol{\Psi}$$

or

$$\mathbf{XX}^T\boldsymbol{\Psi}\boldsymbol{\Lambda} = \mathbf{XX}^T\mathbf{K}^T\mathbf{M}^{-T}\boldsymbol{\Psi}.$$

Assuming $\mathbf{XX}^T$ has full rank, and is invertible, we have

$$\boldsymbol{\Psi}\boldsymbol{\Lambda} = \mathbf{K}^T\mathbf{M}^{-T}\boldsymbol{\Psi}.$$

The assumption that $\mathbf{XX}^T$ is full rank corresponds to a fully multimodal motion with $N \geqq M$ (or a sufficient noise level). Taking the inverse transpose of the above equation,

$$\left[\boldsymbol{\Psi}\boldsymbol{\Lambda} = \mathbf{K}^T\mathbf{M}^{-T}\boldsymbol{\Psi}\right]^{-T}$$

we have

$$\mathbf{K}\boldsymbol{\Psi}^{-T} = \mathbf{M}\boldsymbol{\Psi}^{-T}\boldsymbol{\Lambda}. \tag{4.8}$$

Comparing Eqn. (4.8) with Eqn. (4.3) we see that the SCOD eigenvalues represent the structural eigenvalues, i.e. the modal frequencies squared, and that the matrix of SOD eigenvectors, $\boldsymbol{\Psi}$, and the linear normal modes (LNMs), $\boldsymbol{\Phi}$, of the mass spring system are related as $\boldsymbol{\Phi} = \boldsymbol{\Psi}^{-T}$. These conclusions were reached in [37, 75].

Another relationship worth noting can be shown if we step back to Eqn. (4.8) and let

$\boldsymbol{\Psi} = \mathbf{M}\boldsymbol{\Phi}$. Then

$$\mathbf{K}(\mathbf{M}\boldsymbol{\Phi})^{-T} = \mathbf{M}(\mathbf{M}\boldsymbol{\Phi})^{-T}\boldsymbol{\Lambda}$$

$$\mathbf{K}\mathbf{M}^{-T}\boldsymbol{\Phi}^{-T} = \mathbf{M}\mathbf{M}^{-T}\boldsymbol{\Phi}^{-T}\boldsymbol{\Lambda}.$$

Using symmetry, we have

$$\mathbf{K}\mathbf{M}^{-1}\boldsymbol{\Phi}^{-T} = \boldsymbol{\Phi}^{-T}\boldsymbol{\Lambda}$$

$$\mathbf{M}^{-1}\boldsymbol{\Phi}^{-T} = \mathbf{K}^{-1}\boldsymbol{\Phi}^{-T}\boldsymbol{\Lambda}.$$

Taking the inverse transpose of both sides of the equation and using symmetry,

$$\mathbf{M}\boldsymbol{\Phi} = \mathbf{K}\boldsymbol{\Phi}\boldsymbol{\Lambda}^{-1}$$

$$\mathbf{M}\boldsymbol{\Phi}\boldsymbol{\Lambda} = \mathbf{K}\boldsymbol{\Phi}$$

Therefore, $\boldsymbol{\Psi}$ and $\boldsymbol{\Phi}$ are related through $\mathbf{M}$ as

$$\boldsymbol{\Phi} = \mathbf{M}^{-1}\boldsymbol{\Psi}. \tag{4.9}$$

Another way to see this is to note that, by orthogonality in symmetric systems, $\boldsymbol{\Phi}^T\mathbf{M}\boldsymbol{\Phi} = \mathbf{I}$, which can be manipulated into the equation $\boldsymbol{\Phi}^{-T} = \mathbf{M}\boldsymbol{\Phi}$. By the previous conclusion, that $\boldsymbol{\Psi} = \boldsymbol{\Phi}^{-T}$, we have $\boldsymbol{\Psi} = \mathbf{M}\boldsymbol{\Phi}$. This relationship will be important in the mathematical development of SCOD.

In summary, for linear undamped, symmetric, multimodal free vibration systems, the

two relationships for the eigenvectors of the mass spring system and smooth orthogonal decomposition were just established as $\mathbf{\Psi} = \mathbf{\Phi}^{-T}$ and $\mathbf{\Psi} = \mathbf{M}\mathbf{\Phi}$. Furthermore, the SOD eigenvalues approximate the squares of the modal frequencies. These relationships will be exploited in approximation in experiments, since agreement with the model is an idealization. Smooth complex orthogonal decomposition will be formulated similarly. However, since we will be working with complex analytic signals, the correlation matrices will be generalized as

$$\mathbf{R} = \frac{\mathbf{X}\bar{\mathbf{X}}^T}{N},\tag{4.10}$$

$$\mathbf{S} = \frac{\mathbf{V}\bar{\mathbf{V}}^T}{N},\tag{4.11}$$

where the overbar denotes a complex conjugate. The subtle generalization, in comparison to equations (4.6a) and (4.6b) is the use of the complex conjugate. Since we will be working with a continuous beam, in a later section we will connect the SCOD formulation to distributed parameter vibration models.

4.2   Application of Smooth Orthogonal Decomposition

The application of SCOD involves gathering state measurements. Accelerometers were used in this body of work. After the accelerations are measured the data is post-processed to derive velocities and displacements. The velocities are collected in a velocity ensemble, $\boldsymbol{V}$, and displacements are organized in a ensemble matrix, $\boldsymbol{X}$. The ensembles are organized so each sensor is allocated to a row such that all the data from the ith sensor are in the ith row. Measurement samples are then in each column. For example, $\boldsymbol{X}_{ij}$ contains the ith sensor's

j^{th} sample, for $i = 1, \cdots, M$ and $j = 1, \cdots, N$, where M is the number of sensors and n is the number of time samples.

Typically, the mean of each row is subtracted from each element of that row. The two ensembles are converted to analytic matrices, $\mathbf{Z}$ and $\mathbf{Z}_V$. Next, two correlation matrices are computed, one from the analytic displacements $\boldsymbol{R} = \boldsymbol{Z}\boldsymbol{Z}^T/N$ and the other from analytic velocities $\boldsymbol{S} = \mathbf{Z}_V\mathbf{Z}_V^T/N$. Finally the SCOD eigenvalue problem in the time domain is posed as $\boldsymbol{R}\boldsymbol{\Psi}\boldsymbol{\Lambda} = \boldsymbol{S}\boldsymbol{\Psi}$. Then $\boldsymbol{\Phi} = \boldsymbol{\Psi}^{-H}$ provides an estimate of the modal matrix. The frequencies are the square roots of the diagonals in $\boldsymbol{\Lambda}$. The wavenumbers are computed from the $\boldsymbol{\Phi}$. Each column of $\boldsymbol{\Phi}$ is used to extract a wavenumber where the wavenumber is the gradient of the phase angle.

4.3 Mathematical Development for Smooth Complex Orthogonal Decomposition

In this section we will develop the framework for SCOD in the time domain for distributed parameter systems. Starting with a linear self-adjoint partial differential equation (PDE) for a one-dimensional medium, its eigenvalue problem will be expressed. The SCOD eigenvalue problem will be defined, and then related to the PDE eigenvalue problem. As such, relationships between the eigenvalues and eigenfunctions of SCOD and the PDE eigenvalue problem will be uncovered. But first we will look at the correlation functions in the time domain and make observations about the use of the difference operator in the associated discrete correlation matrices.

Chelidze and Zhou [37] had approximated $\mathbf{V} \cong \mathbf{XD}^T$, where $\mathbf{D}$ is a simple finite difference operator matrix, and had shown that, for SOD,

$$\mathbf{VV}^T \cong \mathbf{XDD}^T\mathbf{X}^T \cong -\mathbf{XA}^T.$$

With this we now turn to SCOD following Eqn. (4.11). Expanding $\mathbf{S} = \mathbf{V\bar{V}}^T/N$ to create the integral form of the correlation matrix starts with

$$\mathbf{S} = \frac{1}{N}
\begin{bmatrix} v_1(t_1) & \cdots & v_1(t_N) \\ \vdots & & \vdots \\ v_M(t_1) & \cdots & v_M(t_N) \end{bmatrix}
\begin{bmatrix} \bar{v}_1(t_1) & \cdots & \bar{v}_M(t_1) \\ \vdots & & \vdots \\ \bar{v}_1(t_N) & \cdots & \bar{v}_M(t_N) \end{bmatrix}$$

such that each element is

$$\mathbf{S}_{ij} = \frac{1}{N} \sum_{k=1}^{N} v_i(t_k)\bar{v}_j(t_k) = \frac{1}{N\Delta t} \sum_{k=1}^{N} v_i(t_k)\bar{v}_j(t_k)\Delta t.$$

Assuming Δt is small and N is large, the limiting integral form is

$$\mathbf{S}_{ij} = \frac{1}{T} \int_0^T v_i(t)\bar{v}_j(t)\, dt, \tag{4.12}$$

where $T = N\Delta T$. Then integrating by parts yields

$$S_{ij} = \frac{1}{T}\dot{x}_i\bar{x}_j\big|_0^T - \frac{1}{T} \int_0^T \ddot{x}_i(t)\bar{x}_j(t)\, dt. \tag{4.13}$$

Since the first term diminishes as T gets large, in the limit we have

$$S_{ij} = -\frac{1}{T} \int_0^T \ddot{x}_i(t) \bar{x}_j(t) \, dt. \tag{4.14}$$

The associated discrete form is

$$S_{ij} = -\frac{1}{N \Delta t} \sum_{k=1}^N a_i(t_k) \bar{x}_j(t_k) \, \Delta t = -\frac{1}{N} \mathbf{A} \bar{\mathbf{X}}^T = -\frac{1}{N} \mathbf{X} \bar{\mathbf{A}}^T, \tag{4.15}$$

the latter of which comes from symmetry in Eqn. (4.12) and the steps that follow.

This suggests that if T is large enough, the form of the difference operator $\mathbf{D}$ does not matter, and generally $\mathbf{V}\bar{\mathbf{V}}^T = -\mathbf{X}\bar{\mathbf{A}}^T$. This also applies for distributed parameter systems.

Starting with the PDE for the beam equation in the linear operator form,

$$m(x)\ddot{u} + Lu = 0 \tag{4.16}$$

where $m(x)$ is the mass per unit length and $u = u(x,t)$ is a function of space and time. We assume $u(x,t)$ is complex and analytic with the form

$$u(x,t) = e^{i\omega t}(c(x) + id(x)) = e^{i\omega t}\phi(x).$$

Taking the partial derivative of $u(x,t)$ with respect to t twice,

$$\frac{\partial^2}{\partial t^2}\{u(x,t)\} = -\omega^2 e^{i\omega t}\phi(x),$$

and substituting it into Eqn. (4.16), leads to the continuous eigenvalue problem

$$L\phi(x) = \omega^2 m(x)\phi(x), \tag{4.17}$$

where the eigenfunction $\phi(x)$ is a complex modal function.

Let $u(x,t)$, $u(y,t)$, $v(x,t)$, and $v(y,t)$ be complex analytic displacement and velocity time signals evaluated at points x and y on the beam and sampled at times $t_k = k\Delta t$ for $k = 1, \cdots, N$. We define

$$R(x,y) = \frac{1}{N} \sum_{k=1}^{N} u(x,t_k)\bar{u}(y,t_k)$$

$$S(x,y) = \frac{1}{N} \sum_{k=1}^{N} v(x,t_k)\bar{v}(y,t_k)$$

where $\bar{u}(y,t_k)$ and $\bar{v}(y,t_k)$ are the complex conjugates. Multiplying inside the summation and dividing outside the summation by Δt gives

$$R(x,y) = \frac{1}{N\Delta t} \sum_{k} u(x,t_k)\bar{u}(y,t_k)\,\Delta t$$

$$S(x,y) = \frac{1}{N\Delta t} \sum_{k} v(x,t_k)\bar{v}(y,t_k)\,\Delta t$$

Letting the Δt become infinitesimal while holding $T = N\Delta t$ fixed results in

$$r(x,y) = \frac{1}{T} \int_0^T u(x,t)\bar{u}(y,t)\,dt \tag{4.18a}$$

$$s(x,y) = \frac{1}{T} \int_0^T v(x,t)\bar{v}(y,t)\,dt. \tag{4.18b}$$

Discretizing spatially, $R_{ij} = r(x_i, y_j)$ and $S_{ij} = s(x_i, y_j)$, and then temporally, leads back to $\mathbf{R}$ and $\mathbf{S}$, defined here for complex analytic signals as

$$\mathbf{R} = \frac{1}{T} \int_0^T u(x_i, t)\bar{u}(y_i, t)\, dt \cong \frac{1}{N}\mathbf{U}\bar{\mathbf{U}}^T \qquad (4.19a)$$

$$\mathbf{S} = \frac{1}{T} \int_0^T v(x_i, t)\bar{v}(y_i, t)\, dt \cong \frac{1}{N}\mathbf{V}\bar{\mathbf{V}}^T \qquad (4.19b)$$

where here $\mathbf{U}$ is the complex displacement ensemble matrix.

The SCOD EVP is $\lambda \mathbf{R}\underline{\psi} = \mathbf{S}\underline{\psi}$ where $\underline{\psi}$ is a discrete eigenvector. We will show that $\underline{\psi}$ approximates a discretization of the system modal functions. The EVP can be written as

$$\lambda \sum_{k=1}^{M} R_{ik}\, \underline{\psi}_k\, \Delta y = \sum_{k=1}^{M} S_{ik}\, \underline{\psi}_k\, \Delta y, \qquad (4.20)$$

where M is the number of measurement points. Eqn. (4.20) can be written as

$$\lambda \sum_{k=1}^{M} r(x_i, y_k)\, \boldsymbol{\psi}(y_k)\, \Delta y = \sum_{k=1}^{M} s(x_i, y_k)\, \boldsymbol{\psi}(y_k)\, \Delta y,$$

and then for a very high spatial resolution and infinitesimal time step, we approach the continuum limit,

$$\lambda \int r(x, y)\psi(y)\, dy = \int s(x, y)\psi(y)\, dy, \qquad (4.21)$$

which is the continuous SCOD in the time domain. Substituting Eqns. (4.18a) and (4.18b) into (4.21) leads to

$$\frac{\lambda}{T} \int_y \left(\int_0^T u(x, t)\bar{u}(y, t)\, dt \right) \psi(y)\, dy = \frac{1}{T} \int_y \left(\int_0^T v(x, t)\bar{v}(y, t)\, dt \right) \psi(y)\, dy. \qquad (4.22)$$

It is desired to express the contents inside the right hand parenthesis as the product of acceleration and displacement as was done in the derivation of discrete SOD. Evaluating x and y at x_i and y_i in Eqn. (4.22) and referring to Eqn. (4.12), we note that the content inside the parenthesis on the right hand side equates to S_{ij}. Using Eqn. (4.14), we can write S_{ij} in terms of the desired product. Hence it is possible to recast Eqn. (4.21) and (4.22) as

$$\frac{\lambda}{T} \int_y \left(\int_0^T u(x,t)\bar{u}(y,t)\, dt \right) \psi(y)\, dy = -\frac{1}{T} \int_y \left(\int_0^T \ddot{u}(x,t)\, \bar{u}(y,t)\, dt \right) \psi(y)\, dy. \qquad (4.23)$$

A subtle but important point should be noted that in Eqn (4.23) the multiplicand has a over-bar, for example the product here is $v(x,t)\bar{v}(y,t)$ and not $v_i v_j$.

Using the symmetry mentioned after Eqn. (4.15), the content of the parenthesis on the right hand side of equation is Hermitian in the continuous sense, such that

$$-\frac{1}{T} \int_0^T \ddot{u}(x,t)\, \bar{u}(y,t)\, dt = -\frac{1}{T} \int_0^T u(x,t)\, \bar{\ddot{u}}(y,t)\, dt.$$

Solving (4.16) for $\ddot{u}$ and substituting into (4.23) brings us to

$$\lambda \int_y \left(\int_0^T u(x,t)\bar{u}(y,t)\, dt \right) \psi(y)\, dy = \int_y \left(\int_0^T u(x,t)\, \frac{L\bar{u}(y,t)}{m(y)}\, dt \right) \psi(y)\, dy.$$

In the next step we will move everything onto one side of the equation, make $\int_y$ the inner

integral, and move all the terms into the inner integral, yielding

$$\int_0^T \int_y \left(\lambda\, u(x,t)\, \bar{u}(y,t)\psi(y) - u(x,t)\frac{1}{m(y)}L\bar{u}(y,t)\,\psi(y) \right) dy\, dt = 0$$

$$\int_0^T u(x,t) \left(\int_y \left[\lambda\, \bar{u}(y,t)\psi(y) - \frac{1}{m(y)}L\bar{u}(y,t)\,\psi(y) \right] dy \right) dt = 0.$$

Applying the adjoint $< Lq, p > = < q, L^*p >$ to move the linear operator, factoring out $\bar{u}(y,t)$, and moving all the terms back into the inner integral produces

$$\int_0^T \int_y u(x,t)\, \bar{u}(y,t) \left(\lambda\, \psi(y) - L^* \left[\frac{\psi(y)}{m(y)} \right] \right) dy\, dt = 0. \tag{4.24}$$

For this equation to have a non-trivial solution, the expression inside of the parenthesis must be equal to zero, producing the following relationship:

$$\lambda\psi(y) = L^* \left[\frac{\psi(y)}{m(y)} \right]. \tag{4.25}$$

If the system is self adjoint, $L^* = L$, and Eqn. (4.25) is rewritten as

$$\lambda\psi(y) = L \left(\frac{\psi(y)}{m(y)} \right). \tag{4.26}$$

Now let

$$\psi(y) = m(y)\phi(y) \tag{4.27}$$

61

to get

$$\lambda m(y)\phi(y) = L\phi(y). \tag{4.28}$$

This shows that ϕ and ψ are related by the mass distribution.

4.4 Simulated Infinite Euler-Bernoulli Beam

The response of an infinite Euler-Bernoulli beam was simulated in the works of [6, 63]. The initial conditions for the beam are

$$
\begin{aligned}
y(x,0) &= f_0 e^{\left(\frac{-x^2}{4b_0^2}\right)} \\
\dot{y}(x,0) &= 0
\end{aligned}
$$

which is a Gaussian distribution on the initial displacement, where $f_0 = 1$ mm and $b_0 = 0.01$ m. The analytical solution to the Euler-Bernoulli beam with the initial condition given above is [6]

$$y(x,t) = \frac{f_0}{(1+a^2t^2/b_0^4)^{1/4}} e^{\left(-\frac{x^2b_0^2}{4(b_0^4+a^2t^2)}\right)} \cos\left(\frac{atx^2}{4(b_0^4+a^2t^2)} - \frac{1}{2}\arctan\left(\frac{at}{b_0^2}\right)\right). \tag{4.29}$$

Simulated Beam Dimensions	
Length	∞
Cross section	0.069 m $\times$ 0.0045 m
Density	7870 kg/m^3
Modulus of elasticity	200 GPa

Table 4.1: Simulated Beam Dimensions

The sensor network on the simulated beam was designed to be the same as the beam

experiment, with identical sensor spacing of $\Delta x = 0.0461$ m over a length of $L = 1.42875$ m, where sensor 1 is located at the origin. However, the sample rate in the simulation was 100,000 Hz, whereas in the beam experiment the sampling rate was 25,000 Hz.

4.4.1 Data Processing

First displacements were computed from the analytical solution from Eqn. (4.29), and the means were subtracted from each "sensor's" time history. Next, using central difference, the velocity ensemble, $\mathbf{V}$, was computed and the means were removed. Central differencing reduces the ensemble matrix dimensions by $2h$, where h is the index interval used in the central difference. So, in order to make each ensemble dimensionally compatible, the first and last h rows of the time samples of displacement were removed from the ensemble. We used $h = 1$. The resulting displacements for sensors 1, 16, and 31 are shown in Figure 4.1. The same plots are also shown for velocities in Figure 4.2. Next, the signals were converted into complex analytic signals by taking the FFT of each row, zeroing out the negative frequencies and multiplying the remaining spectra by two. Finally, the IFFT was applied to obtain the analytic form of $\mathbf{X}$ and $\mathbf{V}$ as $\mathbf{Z}$ and $\mathbf{Z}_v$ respectively.

4.4.2 Results of Simulated Beam

The analytic measurement ensembles were used to create correlation matrices for the SCOD EVP. The natural frequencies were extracted directly from SCOD's eigenvalues, λ, instead of modal coordinate histories as done in the application of COD [46, 76]. The complex modal matrix was computed from the inverse Hermitian transpose of the eigenvector matrix as $\mathbf{\Phi} = \mathbf{\Psi}^{-H}$. The wavenumbers were than computed with a numerical derivative as
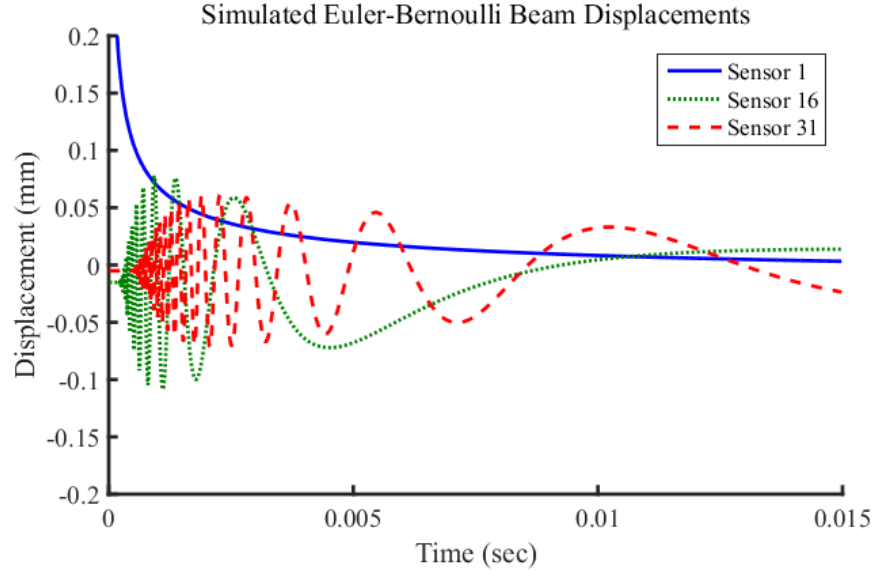
Figure 4.1: Displacements vs. time from the analytical solution for sensor 1, sensor 16, and sensor 31.

$\mathbf{k}_i = d\angle\boldsymbol{\phi}_i/dx$, where $\boldsymbol{\phi}_i$ is a column of the matrix $\boldsymbol{\Phi}$. A forward difference was used along the spatial index of the discretized modal vector in place of the the derivative d/dx. The value of k_i was chosen as the mean value from a spatial interval of uniform values in $\mathbf{k}_i$. The computed modal frequencies versus modal wavenumbers are plotted in Figure 4.3. The least squares fit of the data in Figure 4.3 to the equation $\omega = ak^2$ produced $a_{sim} = 6.52 \text{ m}^2/\text{s}$ compared to $a_{theory} = 6.56 \text{ m}^2/\text{s}$, which is a 0.41% error.

4.5 Results of Beam Experiment

SCOD was applied to the beam experiment, and frequencies were directly computed from the eigenvalues, which saves some computational effort when compared to COD for obtaining frequency information. Samples of SCOMs are shown in Figure 4.4. SCOMs were not whirling as cleanly as COMs for higher modes (see [76] and Chapter 5). The modal wave
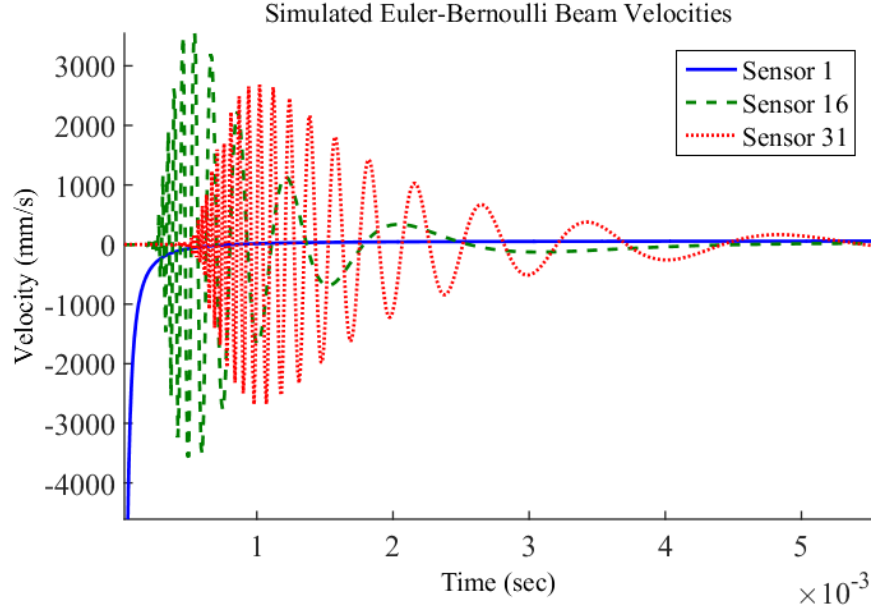
Figure 4.2: Velocities vs. time from finite difference numerical derivatives of the displacements for sensor 1, sensor 16, and sensor 31

numbers were estimated from the whirl rates of the SCOMs, and paired with the associated smooth complex orthogonal values, λ, to obtain the dispersion relationship.

It should be noted that spurious modes are produced when applying SCOD. This is a result of computing the eigenvectors of the SCOD GEVP. Since $\mathbf{R}$ and $\mathbf{S}$ have dimensions $M \times M$, M SCOMs will computed. We can generally expect at most $M/2$ modes. This can be seen by considering a spatial Nyquist criterion if modes are nearly harmonic. Therefore at least $M/2$ SCOMs are expected to be spurious. Furthermore, many modes typically have amplitudes within the level of experimental noise. One can discern the actual modes from the spurious modes by visual inspection. Actual modes will typically be tightly coiled circles or ellipses, while spurious modes tend to look like noise.

Figure 4.4 shows SCOMs extracted from the experimental beam. The top left, top
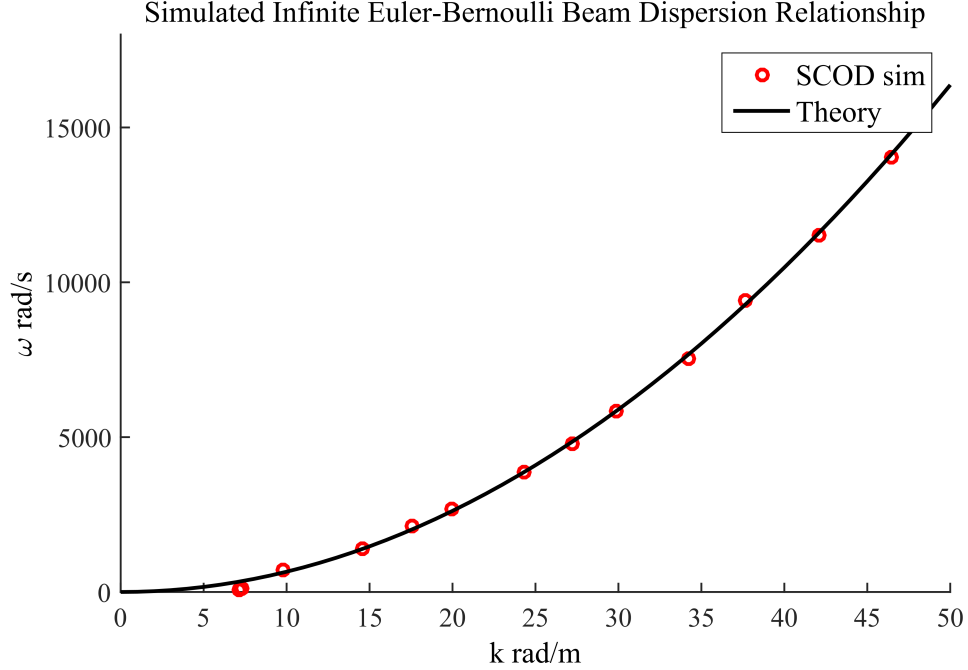
Figure 4.3: Geometric dispersion relation obtained using SCOD for a simulated infinite Euler-Bernoulli beam.

right, and bottom left imagines depict actual SCOMs, the bottom right depicts a spurious mode. SCOD extracts data over a smaller wavenumber range for the same data with similar accuracy, when compared to COD. Figures 4.5, 4.6 and 4.7 show the extracted dispersion relationships when SCOD was applied to the experimental beam data. The group velocities plotted in Figure 4.7 were obtained from a finite difference applied to the dispersion data plotted in Figure 4.5. The least squares approximation of a using the SCOD estimated ω and k gives $a_{SCOD} = 6.72 \ \mathrm{m}^2/\mathrm{s}$, which is an error of 2.6% when compared to $a_{theory} = 6.56 \ \mathrm{m}^2/\mathrm{s}$.

4.6   Conclusions

This paper outlined the mathematical development and application of smooth complex orthogonal decomposition to estimate complex modal characteristics. In using SCOD in
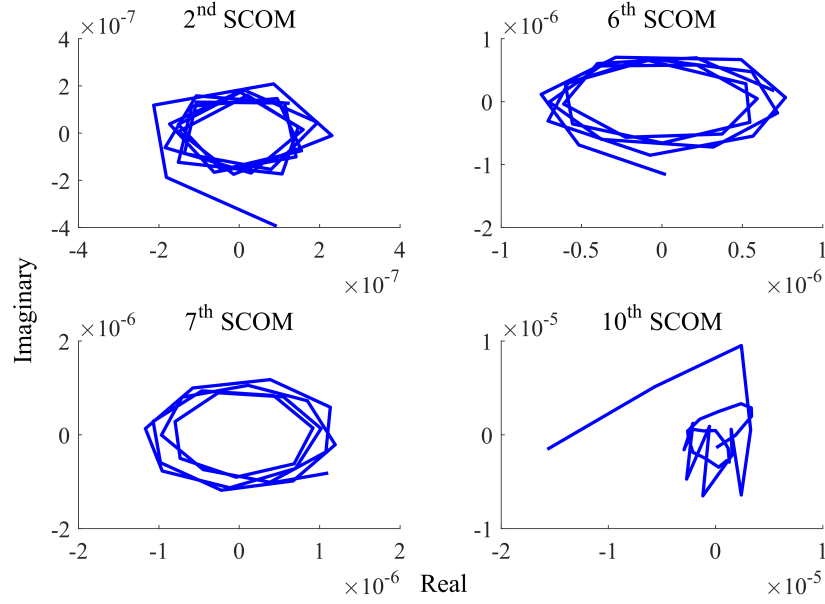
Figure 4.4: Examples of smooth complex orthogonal modes (SCOMs) from the beam experiment. The lower right plot illustrates and example of spurious mode.

the time domain one can directly compute frequencies from the eigenvalues. The complex structural modes are computed from the inverse conjugate transpose of the SCOD eigenvector matrix. For a nearly harmonic traveling complex mode, the wavenumber can be obtained from the gradient of the phase of the mode shape. SCOD was shown to accurately extract modal components of waves traveling through a simulated infinite beam, and an experimental beam. From these modal components, the dispersion properties were accurately extracted.

Currently, efforts are being applied in which SCOD is applied spatially, where displacements and slope or curvature is used, depending on the model's PDE, to extract the parameters of waves propagating in an elastic medium. In contrast to application in the time domain, in which signals are summed (integrated) through time to produce cross correlations between points in space, represented by $\mathbf{R}$ and $\mathbf{S}$, spatial-domain SCOD will involve integrations (sums) of signals through space to produce cross correlations between points in time. Applied

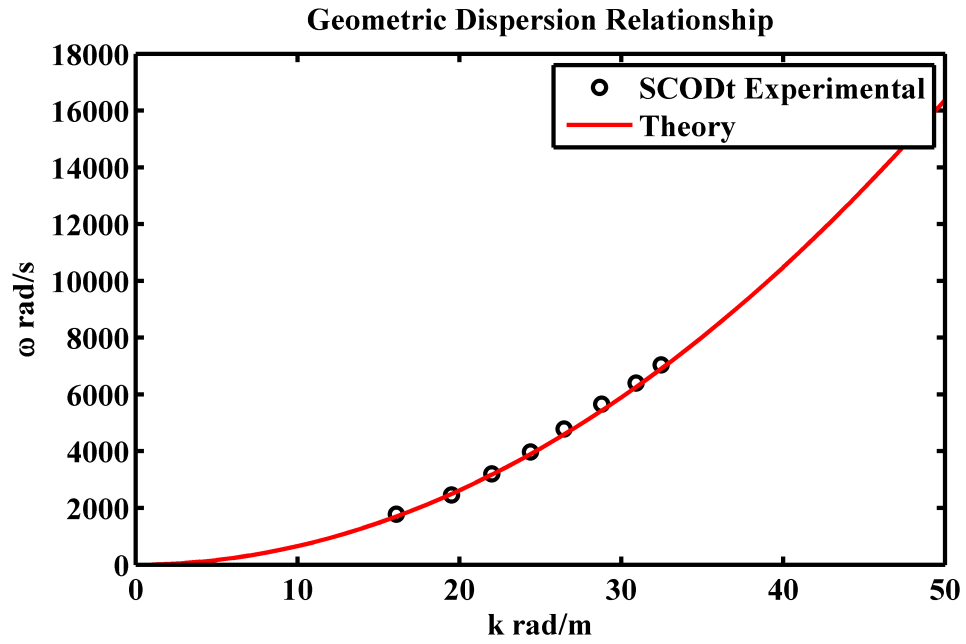Figure 4.5: Dispersion relationship derived from SCOD applied to an experimental beam.

spatially, in some systems wavenumbers are extracted directly from the eigenvalues and the frequencies are extracted from the whirling rates of the temporal eigenvectors.
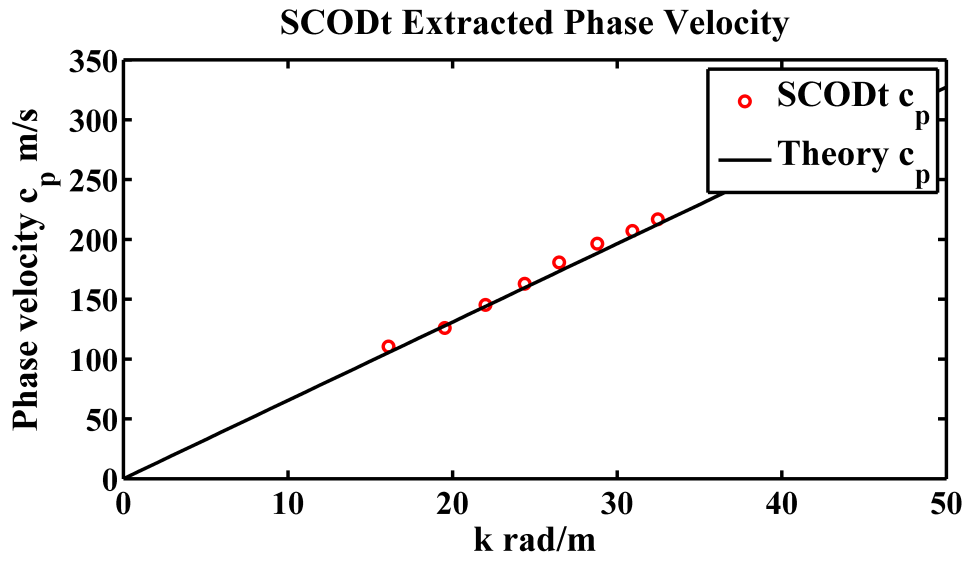
Figure 4.6: Phase Velocity derived from SCOD applied to an experimental beam
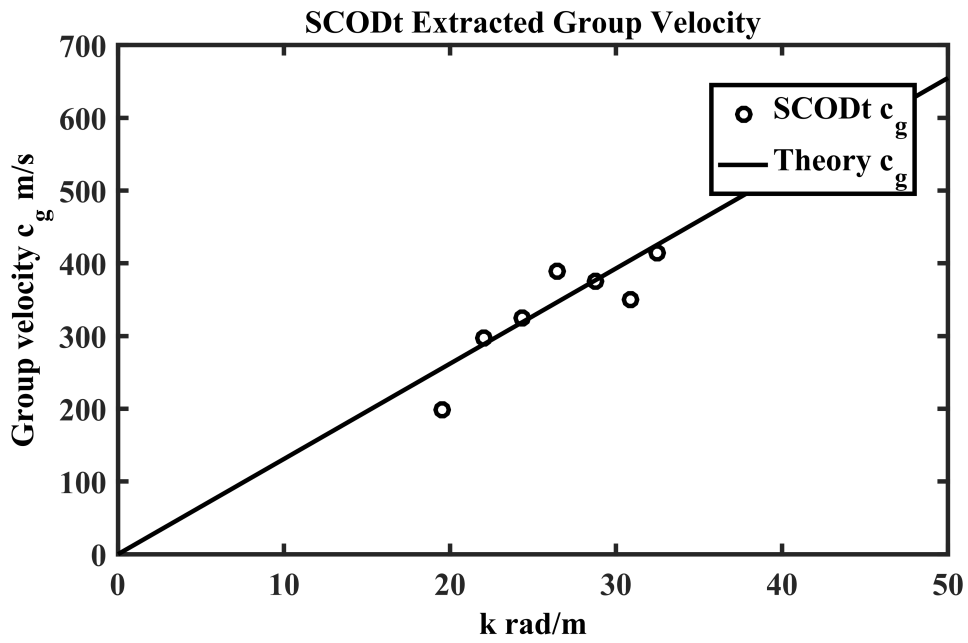
Figure 4.7: Group Velocity derived from SCOD applied to an experimental beam

Chapter 5

Exploration in Spatial Smooth

Complex Orthogonal

Decomposition

5.1   Introduction

COD and SCOD and have been applied to sampled displacements from structures with complex-separable temporal and spatial characteristics. The $M \times N$ sampled ensemble matrices have rows which are time samples of displacements at a certain point on a structure. Thus, the horizontal dimension of the of the ensemble matrix contains the evolution in time, and the vertical dimension contains variations in space. The applications in the previous sections had temporal and spatial behaviors which, when isolated, were approximately harmonic. The temporal application of the COD and complex SCOD involved ensemble matrix products such as $\mathbf{Z}\bar{\mathbf{Z}}^T/N$. These matrix products essentially involve summations through time and produce spatial cross correlations. The result of the COD or SCOD are eigenvectors (modes) which represent spatial optimizations of signal strength (COD) or signal frequency (SCOD), and eigenvalues which represent modal strength (COD) or modal frequency (SCOD). Modal coordinates then contain the temporal modulations of the modes.

In this section we consider inverting the roles of the temporal and spatial variations. Thus, a spatial application of COD and/or SCOD (referred to here as COD-x and SCOD-x) is envisioned such that matrix-product sums are made through space, producing spatial cross correlations between instants in time. The decomposition would thus produce eigenvectors that represent the temporal modulations, and eigenvalues that represent modal strength (CODx) and modal wavenumber (SCODx). The spatial decomposition modal coordinates would contain information about spatial modulation, akin to the usual notion of a mode.

To this end, in this chapter we will introduce smooth complex orthogonal decomposition in the spatial variable domain through an example. In the prior chapter we discussed SCOD in the time domain which provided the ability to directly compute the frequencies from the eigenvalues of the SCOD generalized eigenvalue problem (GEVP). This chapter will illustrate how to extract the wavenumbers directly from the GEVP by posing SCOD spatially. In the next section SCOD will be applied spatially to a traveling pulse, with some mathematical preface in order to illustrate proof of concept.

5.2   Traveling Pulse

SCOD will be applied to a traveling wave whose constituent waves have similar frequencies such that the difference of the maximum and minimum frequencies are small, i.e. $\Delta f = f_{max} - f_{min}$, is small, where $f = \omega/(2\pi)$. In the frequency domain the FFT of the traveling pulse would have a narrow band qualitatively similar to Figure 5.1 [6].

The wave is constructed using $y(x,t) = \sum_{i=1}^{M} A_i \sin(k_i(x - c_0 t))$ where c_0 is the wave speed, $k_i = k_0 + (i-1)\Delta k$, with $k_0 = 4$ and $\Delta k = 0.0472$. The amplitudes A_i are chosen such that the peak of the traveling wave has a value of 1.0. The narrow band traveling pulse
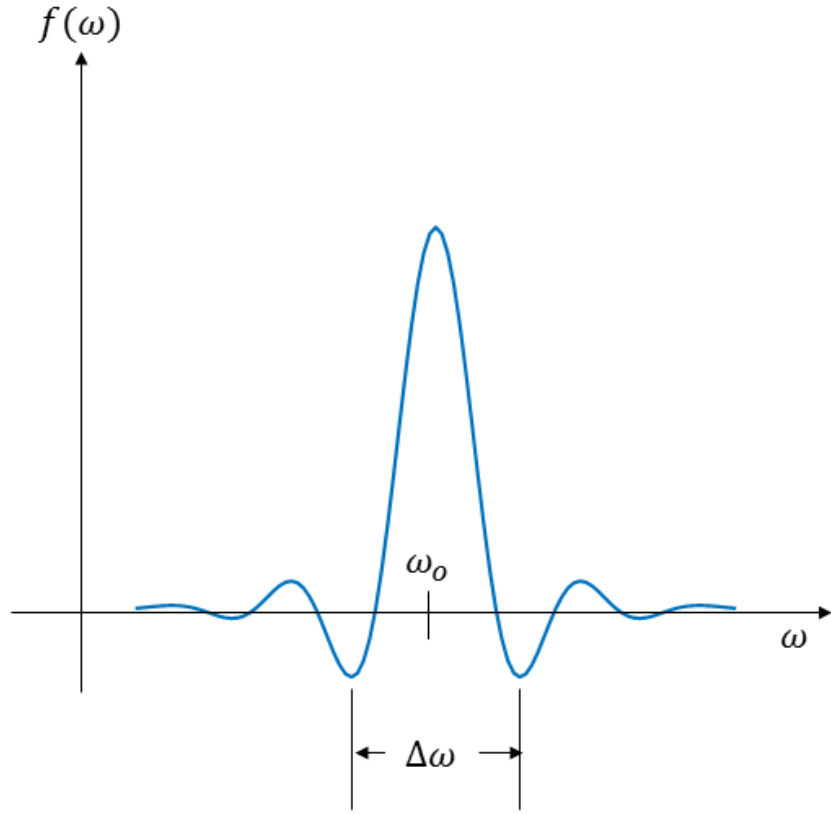
Figure 5.1: Contrived example of the FFT of a narrow band traveling pulse

and the FFT of the traveling pulse at some i^{th} time is shown in Figures 5.2 and 5.3.

An $M \times N$ ensemble matrix was created where N is the number of time samples and M is the number of spatial sensors. For this example $N = M = 128$. The displacement $y(x,t)$ and slope $y'(x,t)$ are sampled to build ensembles $\mathbf{Y}$ and $\mathbf{Y}_{slope}$, which are converted into analytic ensembles $\mathbf{Z}$ and $\mathbf{Z}_V$. $\mathbf{R}$ and $\mathbf{S}$ matrices are computed to produce $N \times N$ matrices

$$\mathbf{R} = \frac{\bar{\mathbf{Z}}^T \mathbf{Z}}{M} \tag{5.1}$$

$$\mathbf{S} = \frac{\bar{\mathbf{Z}}_V^T \mathbf{Z}_V}{M}. \tag{5.2}$$
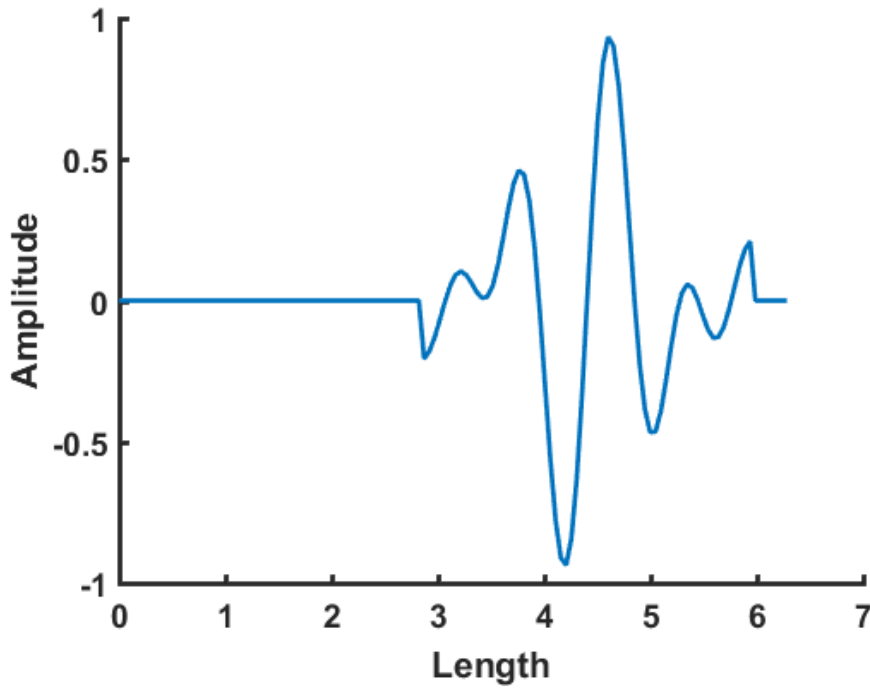
Figure 5.2: Simulated narrow band traveling pulse

The generalized eigenvalue problem is formulated as

$$\mathbf{R V \Lambda = S V} \tag{5.3}$$

where the wavenumbers, k_i, are the square roots of the magnitudes of the eigenvalues, which are the diagonal elements of $\mathbf{\Lambda}$, such that $k_i = \sqrt{||\Lambda_{ii}||}$. Equation (5.3) involves $N \times N$ matrices, and yields $N \times 1$ eigenvectors $\mathbf{v}$, packaged in $N \times N$ matrix $\mathbf{V}$, and N eigenvalues. The "temporal modes", that is the characteristic temporal fluctuations, are represented by columns of the $N \times N$ matrix

$$\mathbf{\Phi}_t = \bar{\mathbf{V}}^{-T} = \mathbf{V}^{-H}, \tag{5.4}$$

much like with the spatial modes from the conventional SCOD in Chapter 4. As such a matrix of "modal coordinates" are calculated from the inverse conjugate transpose of the

73
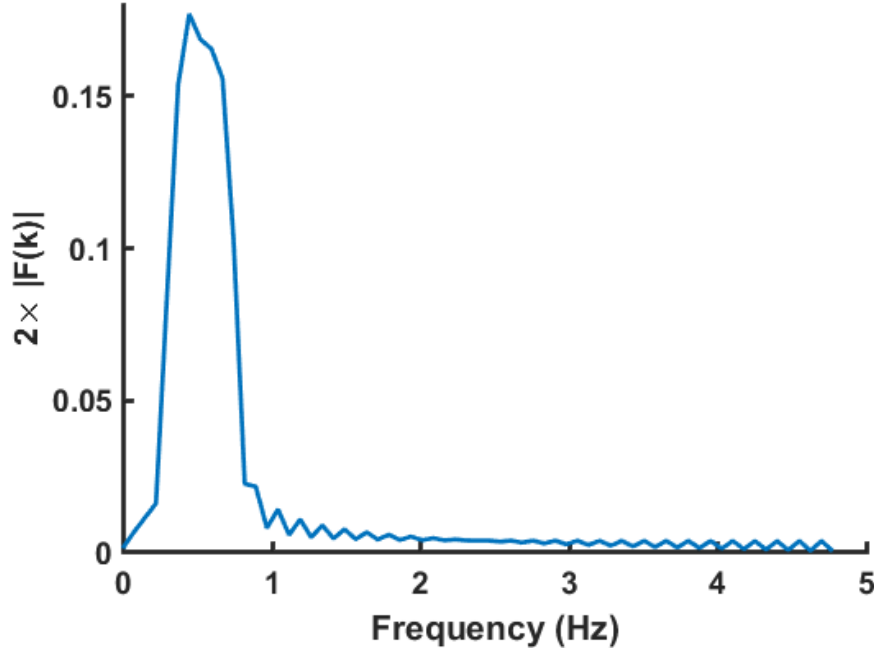
Figure 5.3: FFT of simulated narrow band traveling pulse

eigenvector $\mathbf{V}$, from which the frequencies ω_i can be extracted from the whirl rate of the phase.

In Chapter 4, the complex modal coordinate ensemble was related to the modal matrix and complex analytic displacement ensemble via $\mathbf{Z} = \mathbf{\Phi Q}$, where $\mathbf{\Phi}$ is $M \times M$ and $\mathbf{Q}$ is $M \times N$. Similarly, in terms of the quantities from the SCODx approach, we expect to write

$$\mathbf{Z} = \mathbf{Q}_x \mathbf{\Phi}_t, \tag{5.5}$$

where $\mathbf{Q}_x$ is an $M \times N$ ensemble of "spatial modal coordinates", and are seen as modal coordinates in terms of the computation, but play the role of spatial characteristic shapes. To obtain $\mathbf{Q}_x$, we perform

$$\mathbf{Q}_x = \mathbf{Z}\mathbf{\Phi}_t^{-1} = \mathbf{Z}\bar{\mathbf{V}}^T = \mathbf{Z}\mathbf{V}^H \tag{5.6}$$

74

from equation (5.4). The "spatial modal coordinates" should have "spatial whirl rates", representing wave numbers, consistent with the eigenvalues of Equation (5.3). The "spatial modal coordinates" $\mathbf{Q}_x$ can be used in modal reduction or modal filtering, analogous to what might be done with results from time-domain SCOD.

5.3 Results

SCODx was applied to waves with $c_0 = 1.5$, 3, 6, and 12, and wavenumbers were obtained from the eigenvalues while frequencies were obtained from the whirl rates of the eigenvectors. A least squares fit was applied to the SCODx extracted k_i and ω_i to exact wave speeds of 1.499, 2.99, 5.99, and 11.97. Figures for the extracted dispersion relationship for $c_0 = 1.5$ and $c_0 = 12$ are shown in Figures 5.4 and 5.5.
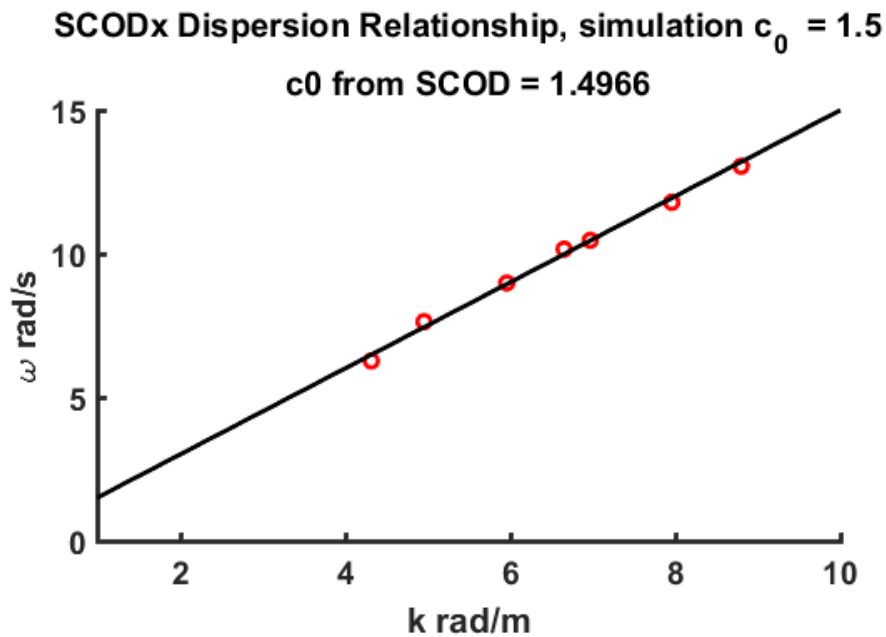
Figure 5.4: Dispersion relationship for a traveling narrow band pulse with a speed of $c_0 = 1.5$

It is believed that a smoother head and tail of the traveling pulse would allow for better dispersion extraction. However the results suggest that for engineering practice with a
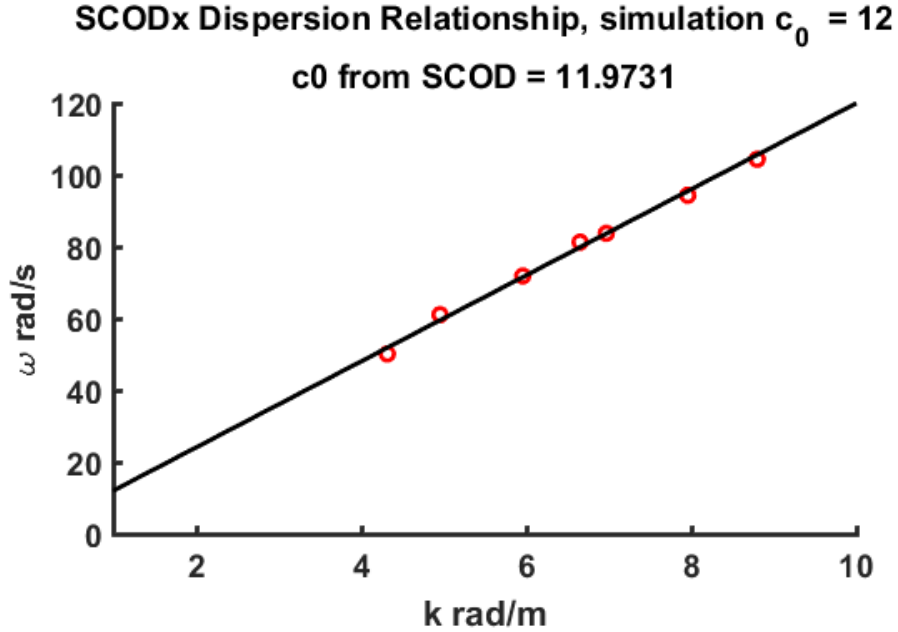
Figure 5.5: Dispersion relationship for a traveling narrow band pulse with a speed of $c_0 = 12$

non-smooth traveling wave, SCODx applied spatially to a narrow band traveling pulse can accurately extract the dispersion relationship and wave speed. While this example is trivial it is a proof-of-concept for SCODx.

5.3.1 Future Works

Future work in SCODx starts with a formulation for a string; SCODx is then to be applied to a simulated string and possibly other structures. The partial differential equation for a uniform string has the form

$$m\frac{\partial^2 u}{\partial t^2} + k\frac{\partial^2 u}{\partial x^2} = 0 \tag{5.7}$$

For the string, axial rod, and torsional rod, the differential operators and independent variables are interchangeable. For example, you could relabel t as x, and x as t, and get the equation

$$m\frac{\partial^2}{\partial x^2} + k\frac{\partial^2}{\partial t^2}u = 0. \tag{5.8}$$

Thus the theory that justified SCOD in the time domain, which included Eqn (5.7), also includes Eqn (5.8), which amounts to SCOD applied in the spatial domain. The pair of equations (5.7) and (5.8) may be a trivial motivating example since, with m and k being constant, the system will not have interesting dispersion characteristics. But SCODx still should work, at least for second-order operators. So a subsequent theory will inquire to what extent this swap in domains" will enable the SCOD in the spatial domain, with a useful interpretation for wave numbers and modal coordinate histories.

Chapter 6

Linear Mass Spring System

6.1 Introduction

In this chapter we will apply complex orthogonal decomposition (COD) [46, 63, 77] and smooth complex orthogonal decomposition (SCOD) [77] for the purpose of extracting the parameters of harmonic complex structural waves traveling through a mass-chain system. When applied, both methods use measurement ensembles to form correlation matrices. COD uses an ensemble of analytic displacement measurements to compute a correlation matrix $\mathbf{R} = \mathbf{Z}\mathbf{Z}^H/N$, where $\mathbf{Z}$ is the analytic displacement ensemble, H is the Hermitian or conjugate transpose, and N is the number of time samples. Next the COD eigenvalue problem (EVP) is posed as $\mathbf{R}\underline{\phi} = \lambda\underline{\phi}$, or in the matrix form $\mathbf{R}\mathbf{\Phi} = \mathbf{\Phi}\mathbf{\Lambda}$. Wavenumbers are computed from the $\underline{\phi}$ as the mean of k_i of $\mathbf{k}_i = d\angle\underline{\phi}_i/dx$, and the frequencies are computed from the modal coordinates, $\mathbf{Q} = \mathbf{\Phi}^{-1}\mathbf{Z}$, as $\omega_i = d\angle q_i/dt$, where q_i is a row of $\mathbf{Q}$.

When using SCOD, a second correlation matrix, $\mathbf{S}$, is built using an analytic ensemble matrix from velocities $\mathbf{Z_v}$, such that $\mathbf{S} = \mathbf{Z_v}\mathbf{Z_v}^H/N$. A SCOD generalized EVP (GEVP) is posed as $\mathbf{R}\mathbf{\Psi}\mathbf{\Lambda} = \mathbf{S}\mathbf{\Psi}$, where $\mathbf{\Lambda}$ is a diagonal matrix of eigenvalues, whose elements provide an estimate of the modal frequencies squared, such that $\mathbf{\Lambda}_{ii} = \boldsymbol{\omega}_i^2$. The wavenumbers are computed similarly as with COD. However, they are computed from $\mathbf{\Psi}$, where columns of

$\mathbf{\Phi} = \mathbf{\Psi}^{-H}$ approximate the mode shapes. The gradient of the angle of each column of $\mathbf{\Phi}$ approximates the associated modal wavenumber.

This paper will focus on applying COD and SCOD to a disturbance propagating through a simulated mass-chain system. The extracted dispersion beavior will be compaed to that predicted by theory. In Section 5.2 the dynamics of the mass-chain system will be summarized. Section 5.3 will apply COD, Rayleigh quotient approximations, and SCOD to the linear mass chain. Finally, we will conclude in Section 5.4.

6.2 Analytical Model for an Infinite Periodic Chain

The wave behavior in an infinite uniform linear mass-spring chain with stiffness α has been studied in detail along with a nonlinear chain in [78, 79]. Here, we show the derivation for a linear chain shown in Figure 6.1.
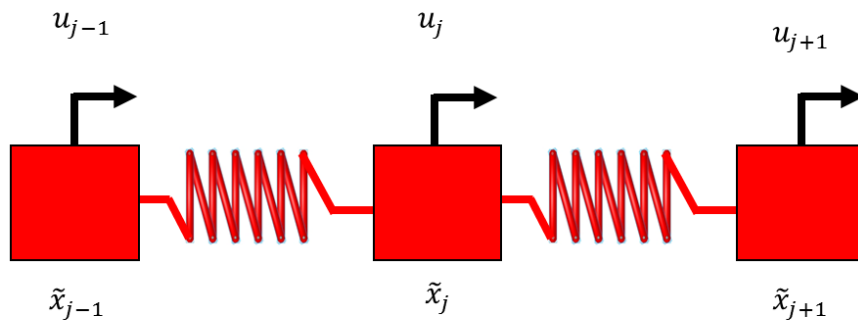
Figure 6.1: Infinite mass chain. The relaxed position and displacement of mass m_j are denoted by $\tilde{x}_j$ and u_j respectively. In this case the springs are linear with relaxed length h.

The mass-spring chain is arranged in a fashion such that each mass is separated by a distance h from its nearest neighbor. h is also the relaxed length of each spring before any deformation occurs. The relaxed position and displacement of mass m_j are denoted by x_j

and u_j respectively. We use the assumption that all the masses are equal $(m_j = m)$ and only the nearest neighbors have direct effects on each other. As such, we consider a linear spring force relative to the equilibrium state. The equations of motion (EOM) in physical coordinates can then be written as

$$m\ddot{u}_j = \tilde{\alpha}\left[(u_{j+1} - u_j) - (u_j - u_{j-1})\right] \tag{6.1}$$

for $j = \cdots, -2, -1, 0, 1, 2, \cdots$. Letting $\alpha = \frac{\tilde{\alpha}}{m}$ we get

$$\ddot{u}_j = \alpha\left[(u_{j+1} - u_j) - (u_j - j - u_{j-1})\right] \tag{6.2}$$

The non-dimensionalization is done by assuming $x = \frac{\tilde{x}}{h}$, which results in $x_j = j$ and $x_{j\pm1} = j \pm 1$. The non-dimensional wave number is denoted by μ. We assume a traveling dispersive wave solution at frequency ω and wave number μ and plug into the equations of motion. Let

$$u_j(t) = Ae^{i(\mu j - \omega t)} + \bar{A}e^{-i(\mu j - \omega t)}. \tag{6.3}$$

Substituting $u_{j\pm1} = e^{\pm i\mu}Ae^{i(\mu j - \omega t)}$ into the equations and balancing leads to

$$\omega^2 = 2\alpha(1 - \cos\mu) \tag{6.4}$$

for the required relationship between ω and μ. This is the dispersion relationship for the linear chain. Thus for a linear chain, the dispersion is given as

$$\omega = \sqrt{2\alpha(1 - \cos\mu)} \tag{6.5}$$
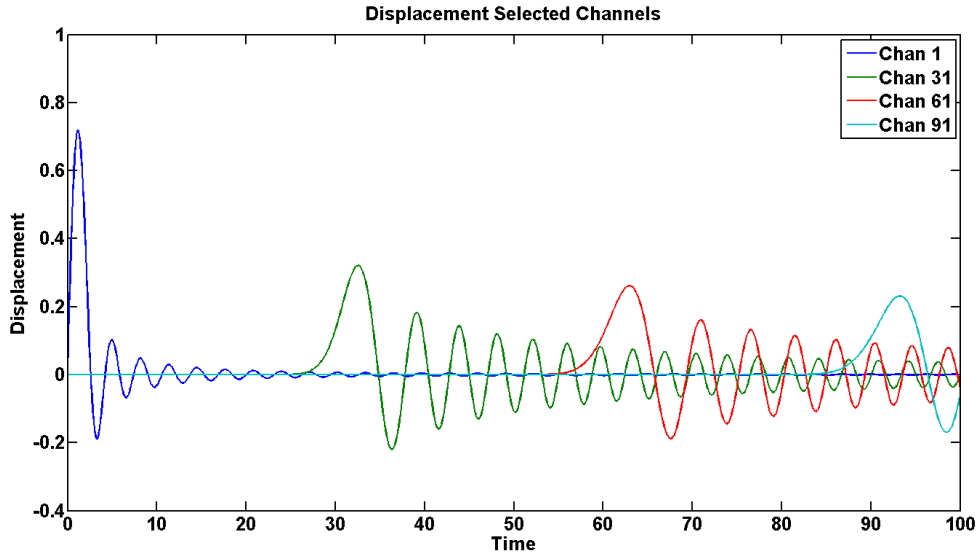
Figure 6.2: Displacements for masses 1, 31, 61, and 91.

6.3   Modal Decomposition Applied to a Mass Chain

A 250 mass mass-spring chain was excited with a unit impulse on the left hand side. The disturbance propagated toward the right. The response of the first 100 masses were recorded as the disturbance passed the 100th mass but before reflections traveled backward to the 100th mass. Essentially, the time record was truncated at a time such that no reflections were recorded. The means were subtracted from the displacements of each mass.

The displacements for four of the masses are shown in Figure 6.2. It can be seen here that the lower frequency waves travel faster than the higher frequency waves, which is consistent with the predicted dispersion behavior of a linear uniform chain. Velocities were also captured for use in SCOD.

81
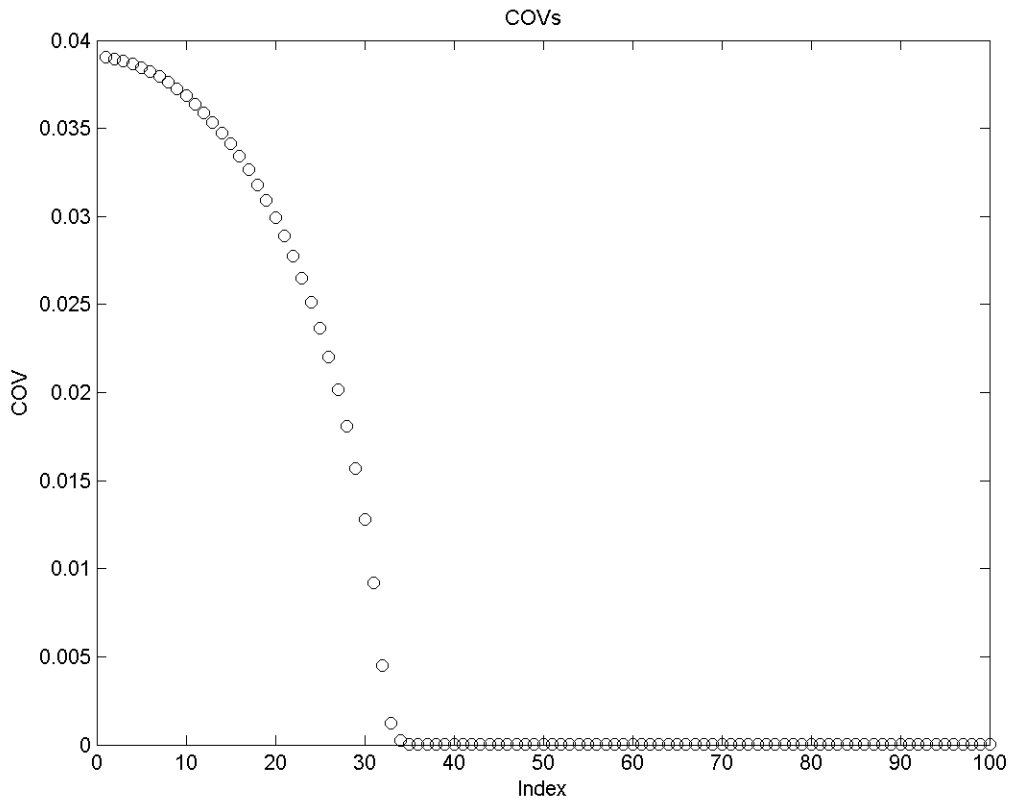
Figure 6.3: Complex orthogonal values
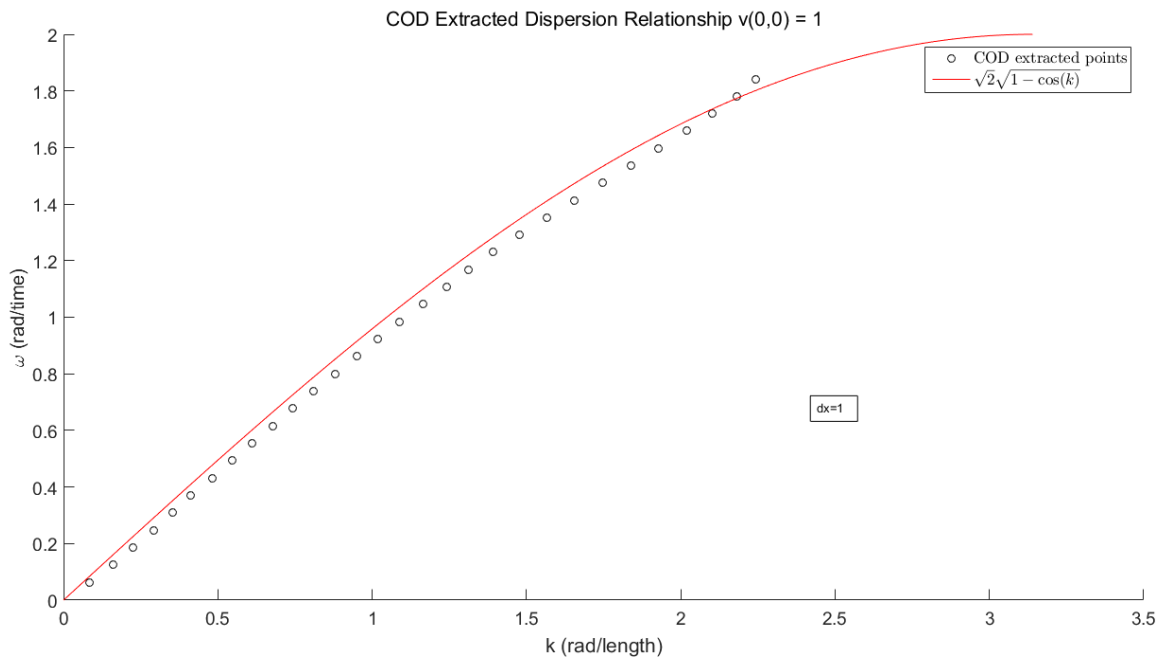
Figure 6.4: Linear system's geometric dispersion relationship using the mode from the 30 highest COVs initial velocity on the first mass = 1.0
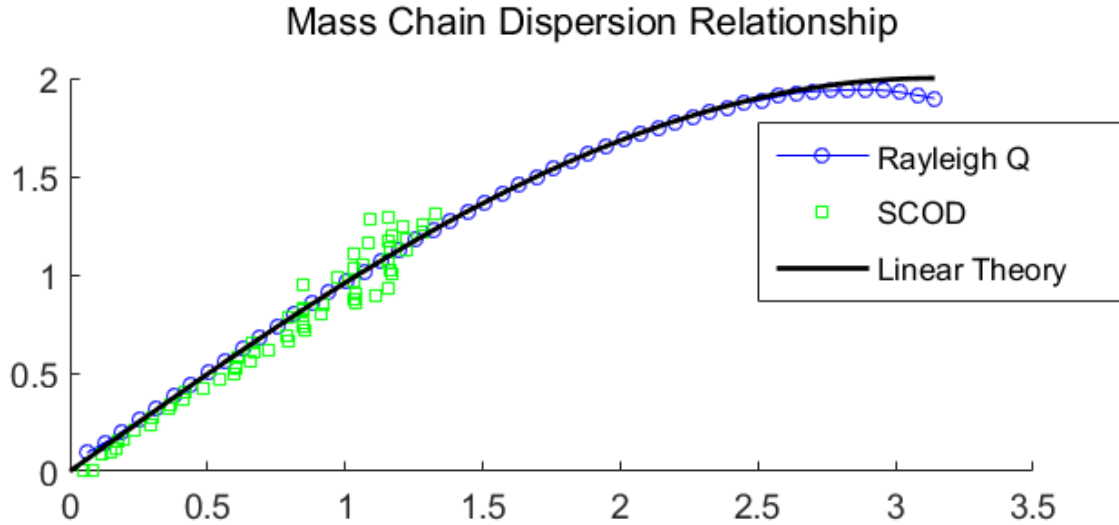
Figure 6.5: Linear dispersion relationship using Rayleigh quotient and SCOD

6.3.1 COD Applied to a Linear Mass Chain

The displacements are converted to complex analytic signals and then used to compute the co-variance matrix, and the COD eigenvalue problem.

The COVs were used as a guide to discern which COMs contained extractable data [44]. The COVs in Figure 6.3 show that about 33 of the extracted modes have significant modal energy. Using the 30 highest COVs the dispersion relationship extracted is shown in Figure 6.4. The COD extracted dispersion relationship correlates well to the theory qualitatively. COD, like POD, has a hard time uniquely extracting modes, and hence wavenumbers and frequencies, when the constituent waves have nearly the same eigenvalue (COV). In order to improve on this we will use assumed modes and the generalized Rayleigh quotient based on the smooth complex orthogonal decomposition, to be discussed next.

6.3.2 SCOD Rayleigh Quotient

The SCOD Rayleigh quotient is based on the SCOD EVP, and is defined as

$$RQ(\lambda) = \frac{\underline{\psi}_a^H \mathbf{R} \underline{\psi}_a}{\underline{\psi}_a^H \mathbf{S} \underline{\psi}_a}. \tag{6.6}$$

$\mathbf{R}$ and $\mathbf{S}$ are the correlation matrices from SCOD, $\underline{\psi}_a$ are columns of a square matrix $\mathbf{\Psi} = \mathbf{\Phi}^{-H}$, where columns of Φ are ϕ_a, and are assumed modes, for this work to be chosen in the form $\phi_a = e^{ikx}$. The value of k can be defined by the user. The Rayleigh quotient will approximate an eigenvalue in the eigenspace of $\mathbf{R}$ and $\mathbf{S}$ when $\underline{\phi}_a$ used as an approximate eigenvector. SCOD correlation matrices were used because the square root of the SCOD eigenvalues are the frequencies of the traveling waves. The results of using the SCOD Rayleigh quotient, in comparison to straight-forward SCOD, can be seen in Figure 6.5.

6.4 Conclusions

The dynamics of an infinite mass-chain were summarized including the dispersion relationship. was solved using the method of multiple scales for a nonlinear mass-chain system. For this work, the elements of $\underline{\phi}_a$ are chosen as $\phi_{aj} = e^{ikx_j}$, consistent with harmonic traveling waves. The chain was simulated with an initial impulse applied to the end mass of a long finite chain. First, COD was applied to the analytic displacements of the masses. COD was able to extract a qualitatively good approximation to the dispersion relationship. SCOD was also applied to obtain an approximation to the lower frequency and lower wavenumber part of the dispersion relation. Improvements were sought by using assumed modes and the generalized Rayleigh quotient. The predicted dispersion relationship using Rayleigh quotients was nearly exact.

Slight deviation was seen near the the origin and near $k = \pi$. Current efforts are underway to apply this method to the linear cubic mass-chain system.

Chapter 7

Conclusions and Future Work

7.1 Summary of Results

COD was successfully applied to a beam experiment with the goal of extracting the dispersion relationship for the beam. The parameters of the beam, data acquisition equipment, and signal processing were outlined so that individuals can repeat the experiment.

The window of minimum and maximum detectable wavenumbers and frequencies were determined by the spatial and temporal Nyquist frequency and record time length criteria. COD, once applied to the measured data, produced nearly harmonic complex waves and modal coordinates within the sampling window. The spatial and temporal whirling rates were obtained from the complex modes and modal coordinates and were used to extract the modal frequencies and modal wavenumbers. From these the dispersion relationship was extracted and matched the theoretical $\omega = ak^2$. Additionally, we were able to anticipate the dispersion curve's shape based on the beam parameters. The coefficient, a, was estimated using a least square fit of the data and was found to be $a_{fit} = 6.4431$ m^2/s, which gives an underestimation of 1.61%. Spurious modes were produced by COD. Actual modes can be discerned from spurious modes by visually inspecting of the whirling complex modes or by the COVs. Spurious modes have very small COVs compared to actual modes.

The mathematical framework for SCOD was outlined and SCOD was applied temporally to both a simulated beam and an experimental beam (the same beam used above and henced data from above). SCOD produced nearly harmonic complex mode and complex eigenvalues. The wavenumbers were computed from the inverse of matrix whose columns were the complex conjugate transpose of the complex modes. The modal frequencies were computed directly from the eigenvalues. The modal frequencies and wave amplitudes can be computed directly from the SCOC. Using the SCOD extracted modal wavenumbers and modal frequencies the dispersion relationship was extracted. Least squares was used to to approximate the coefficient, a. When applied to a simulated beam SCOD extracted least squares fit estimated $a_{sim} = 6.52$ m^2/s which is 0.41% error. SCOD applied to the experimental beam yielded $a_{SCOD} = 6.72$ m^2/s, which is a error of 2.6% when compared to theory.

An exploratory study suggests that it may be feasible to apply COD and SCOD in the spatial domain. In a process referred to as SCODx, the spatial correlation matrices for complex displacements and velocities were computed for the example of a narrow-band pulse. The SCODx eigenvalue problem then produced temporal modes from the eigenvectors and wavenumbers from the eigenvalues. Spatial modal coordinates were also computed to show the strength of modal participation.

Finally, COD, SCOD, and the SCOD Rayleigh quotient were applied to an infinite mass spring system. The chain consisted of 250 masses and only the data from the first 100 masses were recorded. COD was able to extract the dispersion relationship from the mass chain for

a linear system. However, due the the relative closeness of the frequencies of the waves in the mass chain COD has a hard time distinguish the modes of the waves. SCOD was employed and was slightly better at extracting the modes. The best results came from using SCOD Rayleigh quotients with assumed modes.

7.2 Significance

This work presents for the first time an experimental verification of COD applied to a semi-infinite beam. Successful experimental application shows the efficacy of the method, and implies sufficient robustness for real applications.

A mathematical foundation for SCOD was presented showing that SCOD can be considered as a tool for directly obtaining complex normal modes and modal frequencies. SCOD was successfully applied to a simulated semi-infinte beam and an experimental beam. Finally, COD, SCOD, and the SCOD Rayleigh quotient were applied to a mass-chain, which showed COD and SCOD can be applied to a one-dimensional lattice.

This work has applications in sensing, material identification, material property identification, range detection, non-destructive testing and evaluation, and meta-materials.

7.3 Future Works

Future works on these topics includes the application to longitudinal rods, plates, and more complicated structures. These techniques will also be applied when wave reflections are present to see if reflection coefficients and other acoustical boundary properties can be

quantified. We also can consider expanding the method to measure wave attenuation.

CODx and SCODx will be formulated for a rigorous spatial application of modal decomposition methods in systems with operators of justifiable orders. Conditions for the application and interpretation of spatial CODx and SCODx will be understood from this rigorous theoretical formulation. The aim of SCODx will be to generate wave numbers directly from eigenvalues, in place of analyzing modal vectors for their spatial whirl rates. SCOD and SCODx could be used in tandem to obtain, and crosscheck, complete temporal and spatial wave characteristics.

BIBLIOGRAPHY

BIBLIOGRAPHY

[1] Euler, L., 1744. *Methodus inveniendi lineas curvas maximi minimive proprietate gaudentes, sive Solutio problematis isoperimetrici latissimo sensu accepti.* apud Marcum-Michaelem Bousquet & socios.

[2] Bernoulli, D., 1751. "De vibrationibus et sono laminarum elasticarum". *Commentarii Academiae Scientiarum Imperialis Petropolitanae,* **13**, pp. 105–120.

[3] Timoshenko, S. P., 1921. "On the correction for shear of the differential equation for transverse vibrations of prismatic bars". *The London, Edinburgh, and Dublin Philosophical Magazine and Journal of Science,* **41**(245), pp. 744–746.

[4] Fourier, J., 1818. "Note relative aux vibrations des surfaces élastiques et au mouvement des ondes". *Bull. Sci. Soc. Philomathique Paris*, pp. 129–136.

[5] Boussinesq, J., 1885. *Application des potentiels à l'étude de l'équilibre et du mouvement des solides élastiques: principalement au calcul des déformations et des pressions que produisent, dans ces solides, des efforts quelconques exercés sur une petite partie de leur surface ou de leur intérieur: mémoire suivi de notes étendues sur divers points de physique, mathematique et d'analyse*, Vol. 4. Gauthier-Villars.

[6] Graff, K. F., 1975. *Wave Motion in Elastic Solids.* Courier Dover Publications.

[7] Poisson, S.-D., 1828. *Mémoire sur l'équilibre et mouvement des corps élastiques.* L'Académie des sciences.

[8] Rayleigh, L., 1885. "On waves propagated along the plane surface of an elastic solid". *Proceedings of the London Mathematical Society,* **s1-17**(1), pp. 4–11.

[9] Lamb, H., 1904. "On group-velocity". *Proceedings of the London Mathematical Society,* **2**(1), pp. 473–479.

[10] Lamb, H., 1904. "On the propagation of tremors over the surface of an elastic solid". *Philosophical Transactions of the Royal Society of London. Series A, Containing Papers of a Mathematical or Physical Character*, pp. 1–42.

[11] Pao, Y.-H., and Mindlin, R., 1960. "Dispersion of flexural waves in an elastic, circular cylinder". *Journal of Applied Mechanics,* **27**(3), pp. 513–520.

[12] Narasimha, R., 2011. "Kosambi and proper orthogonal decomposition". *Resonance,* **16**(6), June, pp. 574–581.

[13] Chatterjee, A., 2000. "An introduction to the proper orthogonal decomposition". *Current Science,* **78**(7), April, pp. 808–817.

[14] Lumley, J., 1970. *Stochastic Tools in Turbulence.* New York, Academic Press.

[15] Esquivel, P., 2009. "Wide-area wave motion analysis using complex empirical orthogonal functions". In Electrical Engineering, Computing Science and Automatic Control, CCE, 2009 6th International Conference on, IEEE, pp. 1–6.

[16] Liang, Y. C., Lee, H. P., Lim, S. P., Lin, W. Z., Lee, K. H., and Wu, C. G., 2002. "Proper orthogonal decomposition and its applications—part 1: Theory". *Journal of Sound and Vibration,* **252**(3), pp. 527–544.

[17] Berkooz, G., Holmes, P., and Lumley, J., 1967. "The proper orthogonal decomposition in analysis of turbulent flows". *Annual review of Fluid Mechanics,* **25**(539-575), pp. 137 – 146.

[18] Payne, F. R., and Lumley, J. L., 1967. "Large eddy structure of the turbulent wake behind a circular cylinder". *Physics of Fluids (1958-1988),* **10**(9), pp. S194–S196.

[19] Iungo, G., and Lombardi, E., 2011. "Time-frequency analysis of the dynamics of different vorticity structures generated from a finite-length triangular prism". *Journal of Wind Engineering and Industrial Aerodynamics,* **99**(67), pp. 711 – 717. The Eleventh Italian National Conference on Wind Engineering, IN-VENTO-2010, Spoleto, Italy, June 30th - July 3rd 2010.

[20] Bakewell, H. P., and Lumley, J. L., 1967. "Viscous sublayer and adjacent wall region in turbulent pipe flow". *Physics of Fluids (1958-1988),* **10**(9), pp. 1880–1889.

[21] Atwell, J. A., and King, B. B., 2004. "Reduced order controllers for spatially distributed systems via proper orthogonal decomposition". *SIAM Journal on Scientific Computing,* **26**(1), pp. 128–151.

[22] Kunisch, K., Volkwein, S., and Xie, L., 2004. "HJB-POD-based feedback design for the optimal control of evolution problems". *SIAM Journal on Applied Dynamical Systems,* **3**(4), pp. 701–22.

[23] Leibfritz, F., and Volkwein, S., 2006. "Reduced order output feedback control design for PDE systems using proper orthogonal decomposition and nonlinear semidefinite programming". *Linear Algebra and its Applications,* **415**(2), pp. 542–575.

[24] Ly, H. V., and Tran, H. T., 2001. "Modeling and control of physical processes using proper orthogonal decomposition". *Mathematical and Computer Modeling,* **33**(1), pp. 223–236.

[25] Gaonkar, A., and Kulkarni, S., 2015. "Application of multilevel scheme and two level discretization for POD based model order reduction of nonlinear transient heat transfer problems". *Computational Mechanics,* **55**(1), pp. 179–191.

[26] Willcox, K., and Peraire, J., 2002. "Balanced model reduction via the proper orthogonal decomposition". *AIAA Journal,* **40**(11), pp. 2323–2330.

[27] Pironneau, O., 2012. "Proper orthogonal decomposition for pricing options". *The Journal of Computational Finance,* **16**(1), Fall, pp. 33–VI.

[28] Acharjee, S., and Zabaras, N., 2003. "A proper orthogonal decomposition approach to microstructure model reduction in Rodrigues space with applications to optimal control of microstructure-sensitive properties". *Acta Materialia,* **51**(18), pp. 5627–5646.

[29] Galvanetto, U., and Violaris, G., 2007. "Numerical investigation of a new damage detection method based on proper orthogonal decomposition". *Mechanical Systems and Signal Processing,* **21**(3), pp. 1346 – 1361.

[30] Galvanetto, U., Surace, C., and Tassotti, A., 2008. "Structural damage detection based on proper orthogonal decomposition: experimental verification". *AIAA Journal,* **46**(7), pp. 1624–1630.

[31] Banks, H., Joyner, M. L., Wincheski, B., and Winfree, W. P., 2000. "Nondestructive evaluation using a reduced-order computational methodology". *Inverse Problems,* **16**(4), p. 929.

[32] Feeny, B. F., and Kappagantu, R., 1998. "On the physical interpretation of proper orthogonal modes in vibrations". *Journal of Sound and Vibration,* **211**(4), pp. 607–616.

[33] Han, S., and Feeny, B. F., 2002. "Enhanced proper orthogonal decomposition for the modal analysis of homogeneous structures". *Journal of Vibration and Control,* **8**(1), pp. 19–40.

[34] Feeny, B. F., 2002. "On the proper orthogonal modes and normal modes of continuous vibration systems". *Journal of Vibration and Acoustics,* **124**(1), pp. 157 – 160.

[35] Feeny, B. F., and Liang, Y., 2003. "Interpreting proper orthogonal modes in randomly excited vibration systems". *Journal of Sound and Vibration,* **265**(5), pp. 953–966.

[36] Yadalam, V. K., and Feeny, B. F., 2011. "Reduced mass weighted proper decomposition for modal analysis". *Journal of Vibration and Acoustics,* **133**(2), p. 024504.

[37] Chelidze, D., and Zhou, W., 2006. "Smooth orthogonal decomposition-based vibration mode identification". *Journal of Sound and Vibration,* **292**(3-5), pp. 461 – 473.

[38] Bellizzi, S., and Sampaio, R., 2009. "Smooth Karhunen-Loeve decomposition to analyze randomly vibrating systems". *Journal of Sound and Vibration,* **325**(3), pp. 491 – 498.

[39] Farooq, U., and Feeny, B. F., 2008. "Smooth orthogonal decomposition for randomly excited systems". *Journal of Sound and Vibration,* **316**(3-5), Sep, pp. 137–146.

[40] Caldwell Jr., R. A., and Feeny, B. F., 2014. "Output-only modal identification of a nonuniform beam by using decomposition methods". *Journal of Vibration and Acoustics,* **136**(4), May, p. 041010 (10 pages).

[41] Georgiou, I. T., and Papadopoulos, C. I., 2006. "Developing POD over the complex plane to form a data processing tool for finite element simulations of steady state structural dynamics". In International Mechanical Engineering Congress and Exposition, Vol. on DVD-ROM.

[42] Feeny, B. F., 2007. "A complex orthogonal decomposition for wave analysis.". *Journal of Sound and Vibration,* **310**(1), pp. 77–90.

[43] Feldman, M., 2011. "Hilbert transform in vibration analysis". *Mechanical Systems and Signal Processing,* **25**(3), pp. 735–802.

[44] Feeny, B. F., 2002. "On proper orthogonal coordinates as indicators of modal activity". *Journal of Sound and Vibration,* **255**(5), pp. 805 – 817.

[45] Feeny, B. F., and Feeny, A. K., 2013. "Complex modal analysis of the swimming motion of a whiting". *Journal of Vibration and Acoustics,* **135**(2), p. 021004.

[46] Feeny, B. F., 2013. "Complex modal decomposition for estimating wave properties in one-dimensional media". *Journal of Vibration and Acoustics,* **135**(3), p. 031010.

[47] Cox, G. A., Livermore, P. W., and Mound, J. E., 2014. "Forward models of torsional waves: dispersion and geometric effects". *Geophysical Journal International,* **196**(3), pp. 1311–1329.

[48] Hoogstraten, H. W., 1968. "Dispersion of non-linear shallow water waves". *Journal of Engineering Mathematics,* **2**(3), pp. 249–273.

[49] Thomson, W., and Dahleh, M., 1998. *Theory of Vibration with Application 5th Edition.* Prentice-Hall.

[50] Meirovitch, L., 1967. *Analytical Methods in Vibrations.* Macmillan, New York.

[51] Cusumano, J. C., and Bai, B., 1993. "Period-infinity periodic motion, chaos, and spatial coherence in a 10-degree-of-freedom impact oscillator". *Chaos, Solitions, and Fractals,* **3**(5), pp. 515–535.

[52] FitzSimons, P., and Rui, C., 1993. "Determining low dimensional models of distributed systems". *Advances in Robust and Nonlinear Control Systems,* **ASME DSC-VOl. 53**, pp. 9–15.

[53] Azeez, M. F. A., and Vakakis, A. F., 2001. "Proper orthogonal decomposition (POD) of a class of vibroimpact oscillations". *Journal of Sound and Vibration,* **240**(5), Mar, pp. 859–889.

[54] Riaz, M. S., and Feeny, B. F., 2003. "Proper orthogonal decomposition of a beam sensed with strain gages". *Journal of Vibration and Acoustics,* **125**(1), pp. 129 –131.

[55] Kerschen, G., and Golinval, J. C., 2002. "Physical interpretation of the proper orthogonal modes using the singular value decomposition". *Journal of Sound and Vibration,* **249**(5), pp. 849 – 865.

[56] Biglieri, E., and Yao, K., 1989. "Some properties of singular value decomposition and their applications to digital signal processing". *Signal Processing,* **18**, pp. 277–289.

[57] Liu, W., Gao, W. C., and Sun, Y., 2009. "Application of modal identification methods to spatial structure using field measurement data". *Journal of Vibration and Acoustics,* **131**(3), June.

[58] Ibrahim, S., and Mikulcik, E., 1977. "A method for the direct identification of vibration parameters from the free response". *Shock and Vibration Bulletin,* **47**(4), pp. 183 – 198.

[59] Farooq, U., and Feeny, B. F., 2012. "An experimental investigation of a state-variable modal decomposition method for modal analysis". *Journal of Vibrations and Acoustics,* **132**(2), p. 021017 (8 pages).

[60] Feeny, B. F., 1996. "A complex orthogonal decomposition for analyzing wave motion". In ASME International Mechanical Engineering Congress and Exposition, Vol. on DVD-ROM.

[61] Kappagantu, R., and Feeny, B., 1999. "An "optimal" modal reduction of a system with frictional excitation". *Journal of Sound and Vibration,* **224**(5), pp. 863–877.

[62] Önsay, T., and Haddow, A. G., 1994. "Wavelet transform analysis of transient wave-propagation in a dispersive medium". *Journal of the Acoustical Society of America,* **95**(3), pp. 1441–1449.

[63] Feeny, B. F., 2008. "A complex orthogonal decomposition for wave motion analysis". *Journal of Sound and Vibration,* **310**(1–2), Feb, pp. 77–90.

[64] Oppenheim, A. V., and Schafer, R. W., 1989. *Discrete-Time Signal Processing.* Prentice Hall, Englewood Cliffs, NJ.

[65] Schmidt, R., 1986. "Multiple emitter location and signal parameter estimation". *Antennas and Propagation, IEEE Transactions on,* **34**(3), Mar, pp. 276–280.

[66] Roy, R., and Kailath, T., 1989. "ESPRIT-estimation of signal parameters via rotational invariance techniques". *IEEE Transactions on Acoustics, Speech, and Signal Processing,* **37**(7), Jul, pp. 984–995.

[67] Feeny, B. F., Sternberg, P. W., Cronin, C. J., and Coppola, C. A., 2013. "Complex orthogonal decomposition applied to nematode posturing". *Journal of Computational and Nonlinear Dynamics,* **8**(4), p. 041010.

[68] Büssow, R., 2008. "Applications of the flexural impulse response functions in the time domain". *Acta Acustica united with Acustica,* **94**(2), pp. 207–214.

[69] Beck, J., and Arnold, K., 1977. *Parameter Identification in Engineering and Science.* John Wiley and Sons, New York.

[70] Kosambi, D., 1943. "Statistics in function space". *Journal of Indian Mathematical Society,* **7**, pp. 76–88.

[71] Karhunen, K., 1946. "Zur Spektral Theorie Stochastischer Prozesse". *Ann. Acad. Sci. Fennicae,* **A**, pp. 1–34.

[72] Ibrahim, S. R., and Mikulcik, E. C., 1973. "A time domain modal vibration test technique". *Shock and Vibration Bulletin,* **34**(4), pp. 21–37.

[73] Han, S., and Feeny, B. F., 2003. "Application of proper orthogonal decomposition to structural vibration analysis". *Mechanical Systems and Signal Processing,* **17**(5), pp. 989 – 1001.

[74] Brincker, R., Zhang, L., and Andersen, P., 2001. "Modal identification of output-only systems using frequency domain decomposition". *Smart Materials and Structures,* **10**(3), pp. 441–445.

[75] Feeny, B. F., and Farooq, U., 2008. "A nonsymmetric state-variable decomposition for modal analysis". *Journal of Sound and Vibration,* **310**(4-5), March, pp. 792 – 800.

[76] Caldwell, R. A., and Feeny, B. F., 2016. "Characterizing wave behavior in a beam experiment by using complex orthogonal decomposition". *Journal of Vibration and Acoustics,* **138**(4), p. 041007.

[77] Caldwell Jr, R. A., and Feeny, B. F., 2016. "Smooth complex orthogonal decomposition applied to traveling waves in elastic media". In *Rotating Machinery, Hybrid Test Methods, Vibro-Acoustics & Laser Vibrometry, Volume 8*. Springer, pp. 281–293.

[78] Narisetti, R. K., Leamy, M. J., and Ruzzene, M., 2010. "A perturbation approach for predicting wave propagation in one-dimensional nonlinear periodic structures". *ASME Journal of Vibration and Acoustics,* **132**(3), p. 031001.

[79] Narisetti, R. K., Ruzzene, M., and Leamy, M. J., 2011. "A perturbation approach for analyzing dispersion and group velocities in two-dimensional nonlinear periodic lattices". *Journal of Vibration and Acoustics,* **133**(6), p. 061020.